Helios represses megakaryocyte priming in hematopoietic stem and progenitor cells

Giovanni Cova, Chiara Taroni, Marie-Céline Deau, Qi Cai, Vincent Mittelheisser, Muriel Philipps, Matthieu Jung, Marie Cerciat, Stéphanie Le Gras, Christelle Thibault-Carpentier, et al.

JEM Journal of Experimental Medicine

ARTICLE

Helios represses megakaryocyte priming in hematopoietic stem and progenitor cells

Giovanni Cova[1,2,3,4*], Chiara Taroni[1,2,3,4], Marie-Céline Deau[1,2,3,4], Qi Cai[1,2,3,4], Vincent Mittelheisser[1,2,3,4], Muriel Philipps[1,2,3,4], Matthieu Jung[1,2,3,4,5], Marie Cerciat[1,2,3,4,5], Stéphanie Le Gras[1,2,3,4,5], Christelle Thibault-Carpentier[1,2,3,4,5], Bernard Jost[1,2,3,4,5], Leif Carlsson[6], Angela M. Thornton[7], Ethan M. Shevach[7], Peggy Kirstetter[1,2,3,4*], Philippe Kastner[1,2,3,4,8], and Susan Chan[1,2,3,4]

Our understanding of cell fate decisions in hematopoietic stem cells is incomplete. Here, we show that the transcription factor Helios is highly expressed in murine hematopoietic stem and progenitor cells (HSPCs), where it is required to suppress the separation of the platelet/megakaryocyte lineage from the HSPC pool. Helios acts mainly in quiescent cells, where it directly represses the megakaryocyte gene expression program in cells as early as the stem cell stage. Helios binding promotes chromatin compaction, notably at the regulatory regions of platelet-specific genes recognized by the Gata2 and Runx1 transcriptional activators, implicated in megakaryocyte priming. Helios null HSPCs are biased toward the megakaryocyte lineage at the expense of the lymphoid and partially resemble cells of aging animals. We propose that Helios acts as a guardian of HSPC pluripotency by continuously repressing the megakaryocyte fate, which in turn allows downstream lymphoid priming to take place. These results highlight the importance of negative and positive priming events in lineage commitment.

Introduction

Bone marrow (BM) hematopoietic stem and progenitor cells (HSPCs) sit atop a hierarchy that gives rise to all blood cells (Wang and Ema, 2016). They are largely quiescent or slow proliferating and consist of pluripotent long-term (LT) and short-term (ST) hematopoietic stem cells (HSCs), which differ in their ability to self-renew and support lifelong hematopoiesis, as well as multipotent progenitors (MPPs), which contribute to steady-state homeostasis but have limited self-renewal capacity and more restricted lineage potential. MPPs themselves are composed of cells differentially biased toward the platelet/megakaryocyte and erythroid (platelet-multipotent progenitor [P-MPP] and erythroid-multipotent progenitor [E-MPP], collectively part of MPP2), myeloid (myeloid-multipotent progenitor [M-MMP]/MPP3), or lymphoid (lymphoid-multipotent progenitor [L-MPP]/MPP4) cell fates (Oguro et al., 2013; Pietras et al., 2015).

When and how HSPCs become lineage biased is unclear. The classical tree model posited that lineage restriction begins in MPPs (Seita and Weissman, 2010), which make a binary choice to become oligopotent common myeloid progenitors (CMPs) or lymphoid-primed L-MPPs, and then committed megakaryocyte-erythroid progenitors (MEPs), granulocyte-myeloid progenitors (GMPs) or common lymphoid progenitors (CLPs). This model predicted that HSPCs lose lineage potential in discrete steps, with precursors arising late in the hierarchy. Recent studies, however, have suggested that lineage restriction begins in HSCs (Carrelha et al., 2018), where a significant number appear to be megakaryocyte-primed, and express the platelet glycoprotein heterodimeric complex CD41 (encoded by the *Itga2b* gene) and CD61 (encoded by *Itgb3*; Gekas and Graf, 2013; Sanjuan-Pla et al., 2013; Grover et al., 2016). The centrality of the megakaryocyte lineage was revealed by cell tracking experiments, which showed that HSCs generate more megakaryocytes than myeloid or lymphoid cells (Busch et al., 2015; Rodriguez-Fraticelli et al., 2018). Megakaryocyte-biased CD41$^+$ HSCs and pluripotent HSCs have a close cellular relationship and display overlapping transcriptomic profiles and active chromatin signatures (Haas et al., 2015). Interestingly, the numbers of CD41$^+$ platelet-biased HSCs increase with age (Gekas and Graf, 2013; Grover et al., 2016). These studies supported an early split model in which P-MPPs separate first, but they do not explain how these initial steps are regulated or how they might impact the remaining HSPC pool.

[1]Institut de Génétique et de Biologie Moléculaire et Cellulaire (IGBMC), Illkirch, France; [2]Institut National de la Santé et de la Recherche Médicale (INSERM), U1258, Illkirch, France; [3]Centre National de la Recherche Scientifique (CNRS), UMR7104, Illkirch, France; [4]Université de Strasbourg, Illkirch, France; [5]Plateforme GenomEast, Infrastructure France Génomique, Illkirch, France; [6]Umeå Center for Molecular Medicine, Umeå University, Umeå, Sweden; [7]Laboratory of Immune System Biology, National Institute of Allergy and Infectious Diseases, National Institutes of Health, Bethesda, MD; [8]Faculté de Médecine, Université de Strasbourg, Strasbourg, France.

*G. Cova and P. Kirstetter contributed equally to this paper; Correspondence to Peggy Kirstetter: kirstett@igbmc.fr; Philippe Kastner: scpk@igbmc.fr; Susan Chan: scpk@igbmc.fr; P. Kirstetter, P. Kastner, and S. Chan are co-senior authors.

This knowledge is essential if we want to target specific cell lineages during hematopoietic stress or BM transplantations.

The molecular mechanisms responsible for the first steps of lineage commitment remain poorly understood. In the HSC niche, stromal cells and various hematopoietic cell populations communicate via cytokines and cell–cell contact to lineage-priming factors that regulate chromatin accessibility and transcription (Pinho and Frenette, 2019). These signals induce and lock in changes in the gene expression programs associated with lineage bias. Key regulators include the Gata factors (1 and 2) and Runx1, transcriptional activators of the megakaryocyte and erythroid cell fates, as well as Pu.1, required for the development of the myeloid and lymphoid lineages (Wilkinson and Göttgens, 2013).

Helios, encoded by the *Ikzf2* gene, is a member of the Ikaros family of transcription factors. It is a well-known player in regulatory T cell (Treg cell) development and function (Sebastian et al., 2016; Thornton and Shevach, 2019), yet *Ikzf2* mRNA is also highly expressed in HSPCs, suggesting that it may be important for their function. Here, we show that Helios is an essential transcriptional repressor of megakaryocyte priming that helps to maintain pluripotency in HSPCs.

Results

Helios is highly expressed in all HSPCs

To identify the cells expressing Helios in the murine BM, we evaluated the phenotypically defined HSPC populations (CD41$^+$ and CD41$^-$ LT-HSC, ST-HSC, and MPP2-4), committed progenitor cells (GMP, megakaryocyte progenitor [MkP], erythroid progenitor [EryP], and CLP), and mature cell lineages (lymphoid, myeloid, and erythroid) for Helios proteins, by flow cytometry and intracellular staining. Our experiments showed that >99% of HSPCs and ∼80% of committed progenitor cells expressed high levels of Helios (Fig. 1, A, B, and E), suggesting that Helios is active in early hematopoietic cell stages. These results were somewhat unexpected, given that GMPs, MEPs, and CLPs have been reported to express low *Ikzf2* mRNA levels (Drissen et al., 2016; ImmGen Consortium, 2016). Helios proteins were not observed in immature B cells, myeloid cells, and erythrocytes (Fig. 1, C and E), though they were easily detected in a portion of T cells, especially CD4$^+$Foxp3$^+$ Treg cells (Fig. 1, D and E), as reported previously (Sebastian et al., 2016). Indeed, Treg cells expressed the highest levels of Helios in the BM.

To determine if Helios may also play a role in non-hematopoietic BM cells, we analyzed its expression in endothelial cells (ECs) and mesenchymal stem cells (MSCs), the two more abundant populations implicated in HSPC maintenance and differentiation (Fig. 1 F). ECs and MSCs did not express detectable Helios proteins. Thus, Helios is selectively and abundantly expressed in the HSPCs, committed progenitor cells, and Treg cells of the BM.

Helios-null HSPCs skew toward megakaryocytes and away from lymphoid cells

To investigate if Helios influences hematopoiesis, we analyzed the proportions of HSPCs, committed progenitors, and mature lineages in the BM of adult WT and germline Helios-null (KO) mice at different ages (Cai et al., 2009), by flow cytometry. While the BM cellularity was similar between genotypes (Fig. S1 A), multiple HSPC and progenitor populations were affected in the absence of Helios. The biggest increases in the KO BM were observed in the megakaryocyte-biased CD41$^+$ LT-HSC (CD150$^+$CD48$^-$ Lin$^-$Sca1$^+$cKit$^+$ [LSK]), CD41$^+$ MPP2 (CD150$^+$CD48$^+$ LSK), and MkP (CD150$^+$CD41$^+$ Lin$^-$Sca1$^-$cKit$^+$ [LK]) cells (Fig. 2, A–C), at all ages tested (6, 10, and 20 wk). Myeloid-biased populations (MPP3, GMP), as well as BM neutrophils, were also increased (Fig. 2, D and E; and Fig. S1 B), though the results were more variable and less significant. In contrast, the most significant decreases were seen in the lymphoid-biased MPP4 (CD150$^-$CD48$^+$Flt3$^+$ LSK) and CLP (IL7R$^+$Flt3$^+$ Lin$^-$cKit^{med}Sca1^{med}) populations at all ages (Fig. 2, D and F). These differences were due to Helios deficiency and not to alterations in the expression of other Ikaros family members, as Ikaros and Eos were present at similar levels in WT and KO HSPC populations (Fig. S1 C), and Aiolos mRNA and protein were undetectable in all HSPCs (not shown). Far fewer differences were observed in BM lymphocyte and erythroid lineage cells. B lymphocytes (CD19$^+$B220$^+$) were significantly reduced in the KO animals (Fig. S1 D), but the proportions of proB, preB, and immature B cell subsets remained similar between WT and KO (Fig. S1 E). Lastly, both T lymphocytes (CD4$^+$ and CD8$^+$) and erythroid lineage cells (MPP2, EryPs, and erythrocytes) were not overtly affected by Helios loss (Fig. 2, B and G; and Fig. S1, F and G).

To determine if there are functional alterations in the KO progenitor cells, we evaluated the ability of WT and KO BM cells to give rise to megakaryocyte-, myeloid-, and lymphoid-containing colonies in vitro. CFU assays were performed with total BM cells cultured in semi-solid medium supplemented with stem cell factor (SCF), thrombopoietin (TPO), erythropoietin (EPO), interleukin 3 (IL-3), and interleukin 11 (IL-11; for CFU-Megakaryocyte [CFU-Mk] or CFU-Myeloid) or IL-7 (for CFU–preB) for 7 d (Fig. 3 A). Our results showed that KO BM cells gave rise to a higher proportion of CFU-Mk than CFU-Myeloid, compared with WT, and significantly less CFU–preB (Fig. 3, B and C). To dissect the cellular source of these biases, we cultured single LT-HSCs (CD150$^+$CD48$^-$ LSK) in the presence of SCF, TPO, and IL-3 for 10 d to induce the formation of CFU-Mk$^+$ (megakaryocyte-containing) or CFU-Myeloid (Fig. 3 D). KO LT-HSCs gave rise to more CFU-Mk$^+$ and fewer CFU-Myeloid than WT HSCs, suggesting that the KO HSCs are skewed toward megakaryopoiesis. We also evaluated the potential of single cells from the combined myeloid- and lymphoid-biased MPP population (CD150$^-$CD48$^+$ LSK) to form CFU-Myeloid after 7 d in culture with SCF, EPO, IL-3, and IL-6, which showed that KO cells gave rise to significantly more myeloid colonies (Fig. 3 E). These results indicated that myelopoiesis decreases in HSCs but increases in MPPs upon Helios loss.

Thus, Helios-null HSPCs give rise to more megakaryocytes and fewer lymphoid cells than WT HSPCs under permissive conditions.

Helios affects adult HSPC differentiation in a cell-intrinsic manner

To determine if Helios directly affects HSPCs, we tested the ability of BM MPPs and LT-HSCs to repopulate the hematopoietic system after transplantation into recipient mice. To evaluate

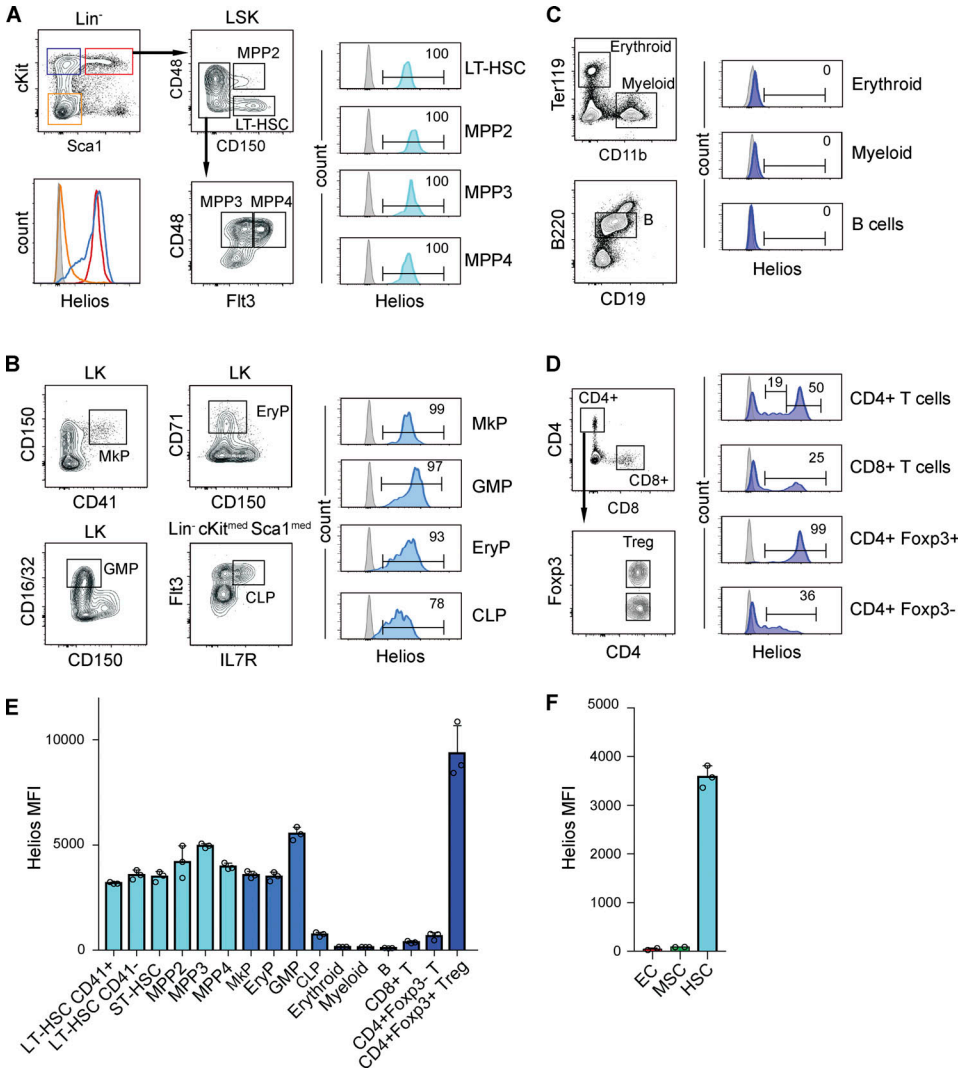

Figure 1. **Helios is highly expressed in HSPCs. (A–D)** Representative gating strategies and Helios expression in BM hematopoietic cell populations. The gray histograms correspond to total BM cells stained with the secondary Ab alone. In A, the LSK ($Lin^-Sca1^+cKit^+$, red gate), LK ($Lin^-Sca1^-cKit^+$, blue gate), and $Lin^-Sca1^-cKit^-$ (orange gate) cells are indicated. Numbers correspond to percentages. The indicated HSPC populations are as follows: LT-HSC, $CD48^-CD150^+$ LSK; MPP2, $CD48^+CD150^+$ LSK; MPP3, $CD48^+CD150^-Flt3^-$ LSK; MPP4, $CD48^+CD150^-Flt3^+$ LSK; MkP, $CD150^+CD41^+$ LK; GMP, $CD150^-CD16/32^+$ LK; EryP, $CD71^+$ LK; CLP, $Lin^-cKit^{med}Sca1^{med}Flt3^+IL7R^+$. The mature cell populations are as follows: erythroid, $Ter119^+CD71^+CD11b^-$; myeloid, $CD11b^+B220^-Ter119^-$; B cell, $B220^+CD19^+$; $CD4^+$ T cell, $CD4^+CD8^-$; $CD8^+$ T cell, $CD4^-CD8^+$; Treg cell, $CD4^+Foxp3^+$; non-Treg T cell, $CD4^+Foxp3^-$. **(E)** Helios median fluorescence intensity (MFI) in the indicated populations. Light blue bars indicate HSPC populations. Medium blue bars indicate committed progenitors. Dark blue bars indicate mature cells. **(F)** Helios MFI in BM non-hematopoietic cells: EC, $CD45^-NG2^-CD31^+$; MSC, $CD45^-NG2^+CD31^-$; total LT-HSCs as positive control. In E and F, mean ± SD of two to three independent experiments.

MPP function, 5×10^3 MPP3 or MPP4 cells from WT or Helios-KO mice ($CD45.2^+$) were injected i.v. into sublethally irradiated recipients ($CD45.1^+CD45.2^+$), and blood was analyzed after 2 wk for $CD45.2^+$ $B220^+$ B, and $CD11b^+$ myeloid cells (Fig. 4 A). When MPP3 cells were injected, both WT and KO genotypes gave rise exclusively to myeloid cells. In contrast, when MPP4 cells were injected, WT cells were biased toward the B cell lineage, as expected, but KO cells were almost equally divided into B and myeloid cells, indicating a loss of lymphoid potential, like that seen in vitro.

To evaluate LT-HSC function, we injected 100 WT or KO LT-HSCs ($CD45.2^+$) along with 5×10^5 supporting WT BM cells ($CD45.1^+$) into lethally irradiated mice ($CD45.1^+CD45.2^+$; Fig. 4 B). Blood cells were analyzed after 2 mo for $CD45.2^+$ $B220^+$ B, $CD3^+$ T, and $CD11b^+$ myeloid cells. We observed a similar relative decrease in B cells and increase in myeloid cells in recipients that had received KO HSCs compared with WT. However, the T cell contribution was similar between WT and KO HSCs, suggesting that T cell development was not grossly affected by Helios deficiency. These results showed that Helios-null LT-HSCs and MPP cells give rise to proportionately fewer B cells in a cell-intrinsic manner.

Because the Helios KO mutation is germline, we asked if Helios loss in the adult similarly affects HSPC differentiation. Mice carrying *Ikzf2* floxed alleles were crossed with Rosa-CreERT2$^+$ animals, and WT (Ikzf2$^{f/f}$ Rosa-CreERT2$^-$) and

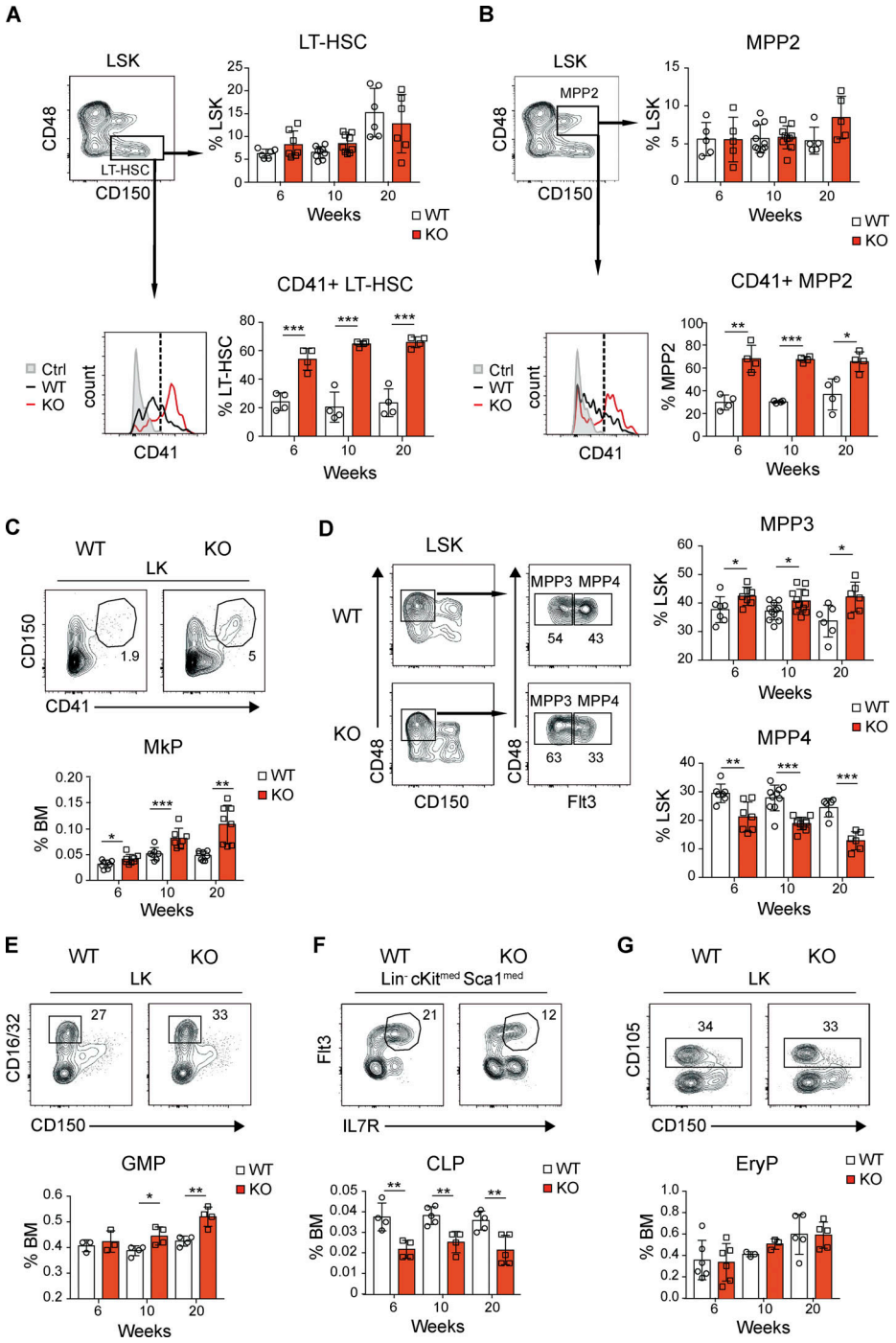

Figure 2. **Helios deficiency affects BM megakaryocyte and lymphoid progenitor frequencies. (A–G)** Relative abundance of the indicated BM populations in WT and KO mice at 6, 10, and 20 wk of age. Representative contour plots and statistical significance are shown. In the histograms of D and E, the control histogram shows the CD41 level of WT MPPs ($CD48^+CD150^-$ LSK). Numbers in the plots correspond to percentages. Each data point corresponds to one mouse; mean ± SD are shown per population for four to eight mice from multiple independent experiments. Unpaired two-tailed *t* test: *, $P < 0.05$; **, $P < 0.01$; ***, $P < 0.001$.

conditional KO (cKO; $Ikzf2^{f/f}$ Rosa-CreERT2$^+$) mice were injected with tamoxifen for 5 d to delete *Ikzf2* (Fig. 4 C). HSPCs were analyzed 3 wk after the first injection. Helios expression was comparable between cKO and germline KO LSK cells, indicating efficient deletion. Strikingly, the HSPC phenotype was reproduced in the treated cKO animals, where there was a clear and significant increase in the percentages of $CD41^+$ LT-HSCs, $CD41^+$ MPP2 and MPP3 cells, and a corresponding decrease in the MPP4 population. These results demonstrated that Helios continuously represses megakaryocyte commitment and promotes lymphopoiesis over myelopoiesis in the adult BM, a function that is rapidly reversed upon Helios deletion.

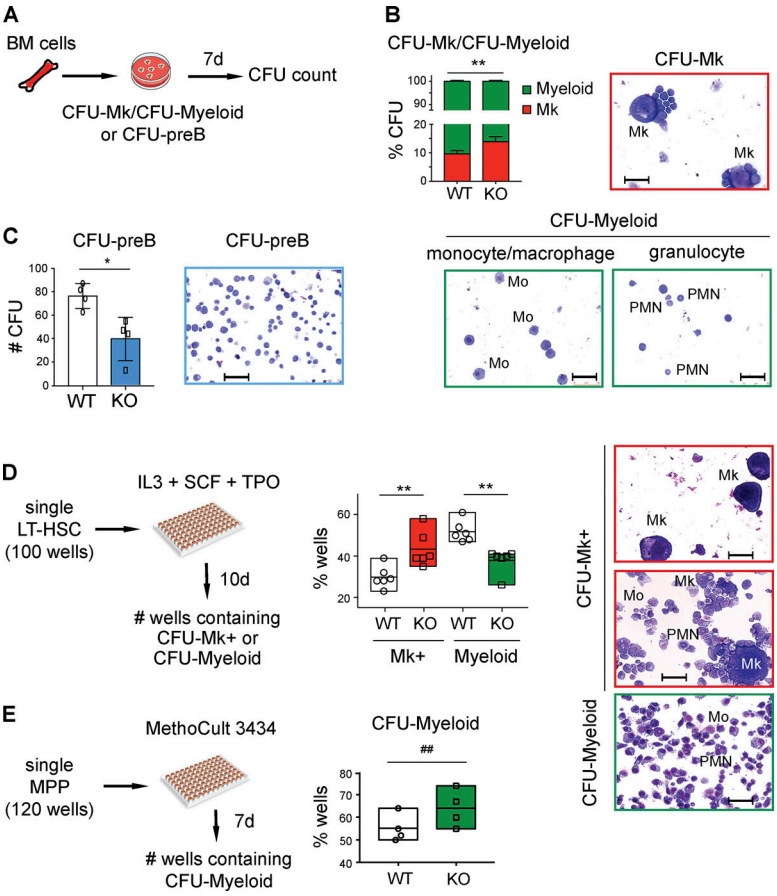

Figure 3. **In vitro differentiation of Helios KO HSPCs.** **(A)** Strategy of CFU-Mk/CFU-Myeloid and CFU–preB assays. **(B)** Ratios of CFU-Mk and CFU-Myeloid (granulo-monocyte) from 5 × 10^4 BM cells seeded after 7 d. Mean ± SD of four independent experiments. Representative MGG staining of different colonies are shown. **(C)** Number of CFU-preB from 15 × 10^4 BM cells seeded after 7 d. Each data point represents the mean of duplicate cultures for each mouse. Mean ± SD of four independent experiments. Representative MGG staining of preB cell colonies shown. **(D)** Strategy of single-cell LT-HSC cultures (left). 100 wells were seeded for each sample. Percentage of wells containing CFU-Mk^+ or CFU-Myeloid after 10 d is indicated. Boxes represent the mean ± SD of six independent experiments. Representative MGG staining of colonies are shown. **(E)** Strategy of single-cell MPP cultures (left). 120 wells were seeded for each sample. Percentage of wells containing CFU-Myeloid after 7 d is indicated. Boxes represent the mean ± SD of four independent experiments. Mk, megakaryocyte; Mo, monocyte/macrophage; PMN, polymorphonuclear granulocyte. Scale bars correspond to 50 µm. Unpaired two-tailed *t* test: *, P < 0.05; **, P < 0.01. Paired two-tailed *t* test: ##, P < 0.01.

Helios regulates HSPC function independently of T cells and external factors

We observed that the Helios-KO BM contained fewer $CD4^+CD25^+Foxp3^+$ Treg cells, and more $CD4^+Foxp3^-$ T cells producing IFNγ, IL-2, and IL-10, than WT BM (Fig. S2, A and B). This, together with an increase in $CD41^+$ LT-HSCs, suggested chronic inflammation in the KO BM (Haas et al., 2015; Mirantes et al., 2014). To test if Treg deficiency impacted HSPC function, we studied hematopoiesis in $Ikzf2^{f/f}$ CD4-Cre^+ T cell KO (TKO) mice (Fig. 5 A), where Helios was specifically deleted in T cells (Sebastian et al., 2016; Hirata et al., 2018). If Helios-expressing T cells were responsible for the HSPC bias in germline KO BM, we reasoned that a similar bias would be observed when Helios was deleted only in T cells. On the other hand, if the hematopoietic defect was intrinsic to HSPCs, then we would see no defects in hematopoiesis. Indeed, the latter case was true, as WT ($Ikzf2^{f/f}$ CD4-Cre^-) and TKO mice had similar percentages of BM hematopoietic populations. Thus, Helios-proficient HSPCs are not affected by Helios loss in T cells.

To determine if Helios KO mice can still respond to stress-induced megakaryopoiesis, we measured the ability of WT and KO animals to increase their CD41-expressing HSPC numbers following TLR3 activation by polyinosinic:polycytidylic acid (poly I:C) injection (Haas et al., 2015), a treatment that does not appear to influence Helios protein levels in WT mice (not shown). Both WT and KO mice increased their proportions of $CD41^+$ LT-HSCs and MPP2 cells, as well as their levels of CD41 expression per cell, after treatment (Fig. S2 C). In contrast, the ST-HSC phenotype stayed unchanged. These results demonstrated that both WT and KO HSPCs are capable of responding to stress and suggested that KO animals begin with an advantage because they start with and maintain a larger pool of $CD41^+$ HSCs biased toward the megakaryocyte lineage.

To determine if HSPCs are influenced by neighboring hematopoietic cells, we performed competitive transplantation experiments with WT and KO cells. Lethally irradiated recipient mice ($CD45.1^+CD45.2^+$) were reconstituted with WT or KO BM cells ($CD45.2^+$) and competitor WT BM cells ($CD45.1^+$) at a 1:1 ratio (Fig. 5 B). After 2 mo, $CD45.2^+$ and $CD45.1^+$ blood cells were analyzed for $B220^+$ B and $CD11b^+$ myeloid cells. These results showed that KO donor cells (in red) exhibited the same relative loss of B cell potential (and gain of myeloid) even in the presence of WT BM cells. On the other hand, WT competitor HSPCs retained their normal potential (compare the gray data points between the left and right graphs).

These results demonstrated that Helios regulates the developmental potential of HSPCs in a cell-autonomous manner independently of T cells and the microenvironment.

Helios represses a megakaryocyte gene expression program in HSPCs

To determine how gene expression is regulated by Helios, we analyzed the gene expression changes between WT and Helios KO LT-HSCs ($CD150^+CD48^-$ LSK), MPP3 cells ($CD150^-CD48^+Flt3^-$ LSK), and MPP4 cells ($CD150^-CD48^+Flt3^+$ LSK) by RNA sequencing

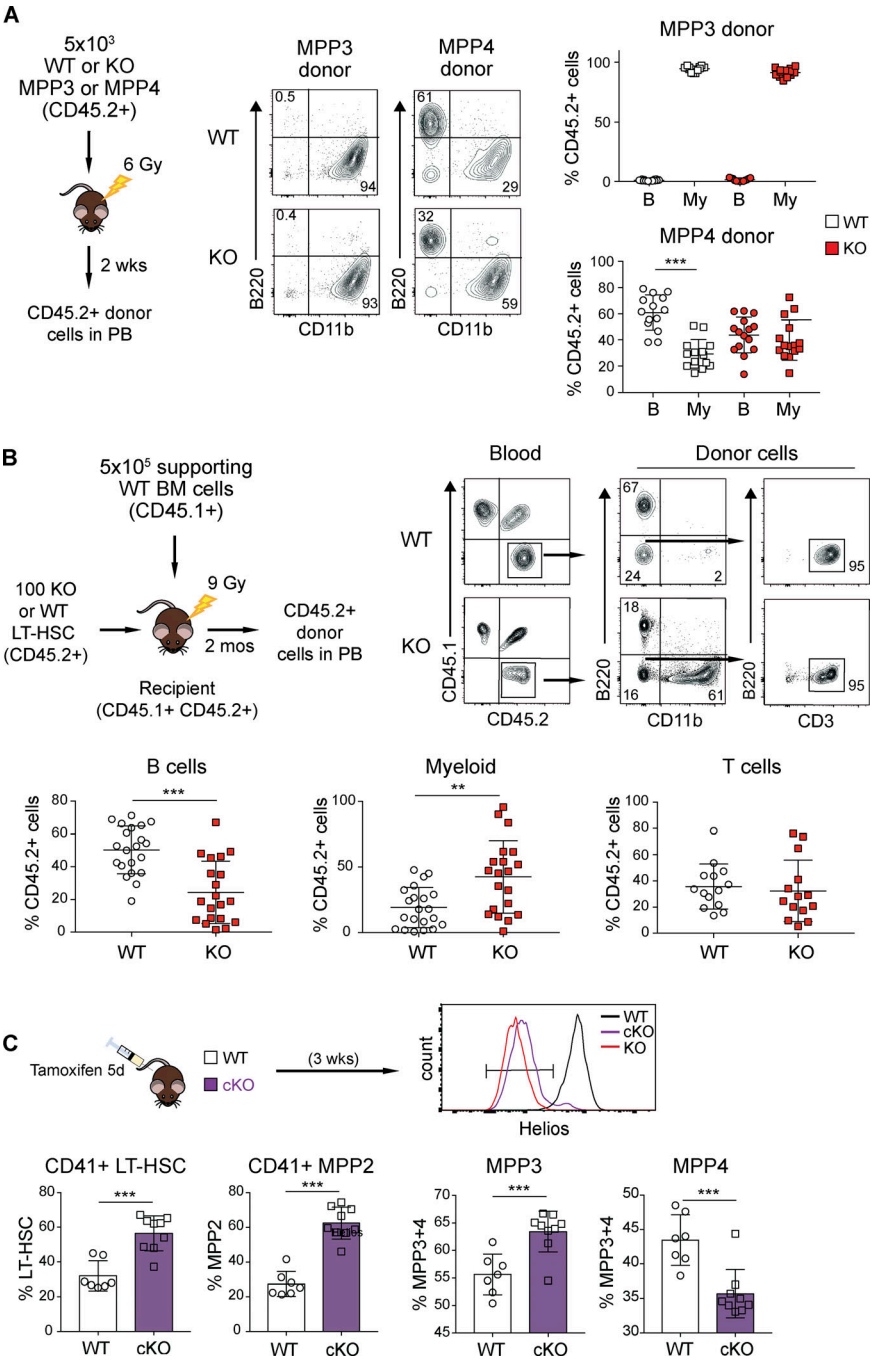

Figure 4. **In vivo lymphoid potential of Helios KO HSPCs. (A)** Strategy of MPP transplantation (left). Representative contour plot of peripheral blood cell staining (middle). Numbers correspond to percentages. Mean ± SD of four independent experiments with three to five recipient mice per donor genotype (right). Each data point represents the percentage of donor cells per recipient. B, B220⁺ cells; My, CD11b⁺ cells. **(B)** Strategy of LT-HSC transplantation (top left). Representative contour plot of peripheral blood cell staining (top right). Numbers correspond to percentages. Mean ± SD of two (T cells) or three (B and myeloid cells) independent experiments, with six to eight recipient mice per donor genotype (bottom). Each data point represents the percentage donor cells per recipient. **(C)** HSPC phenotype of Helios cKO mice. Top: Flow cytometry analysis of Helios expression in LSK cells from WT, KO, and cKO mice, analyzed 3 wk after tamoxifen-induced Ikzf2 inactivation. Bottom: Analysis of the indicated BM populations in WT and cKO mice. Mean ± SD of four independent experiments with seven to nine mice per genotype. Unpaired two-tailed test: **, P < 0.01; ***, P < 0.001.

(RNA-seq; Fig. 6 A and Table S1). Most of the changes (n = 419) were found between WT and KO LT-HSCs, with fewer differences in the MPP3 and MPP4 subsets. Gene set enrichment analysis (GSEA) indicated that genes associated with a MkP signature (*Selp*, *Cd9*, *Vwf*, *Itgb3*, and *Plek*) were highly enriched within the up-regulated genes in the KO LT-HSCs compared with WT, while those associated with a lymphoid-biased MPP4 signature (*Cd52*, *Ccr5*, and *Clec12a*) were diminished (Fig. 6, A and B). Similar biases were observed in the MPP3 and MPP4 populations, where the MkP signature was enriched and the MPP4 and CLP signatures were reduced (Figs. 6 C and S3 A). Metascape pathway analysis confirmed the up-regulation of genes involved in platelet activation (Fig. 6 D). Interestingly, the down-regulated genes included those involved in cell migration and associated processes, like the regulation of focal adhesion (*Atat1*, *Cxadr*, and *Tiam2*), cilium assembly (*Mks1*, *Lca5*, *Ccdc181*, *Ift80*, and *Wdr35*), and cytoskeleton function (*Utrn*, *Ssh2*, *Cttnbp2*, and *Afap1*), which suggested that Helios KO HSCs are less motile in the BM environment. Of note, the above genes were selected (adjusted P value [adj P] < 0.2) to accommodate the natural variability in gene expression between mice. This criterion alone appeared to filter out most of the noise, as it was met by few genes (n = 75) in the MPP4 population. Further, the genes selected with mild (0.05< adj P < 0.2) and stringent (adj P < 0.05) criteria identified similar pathways, such as cell migration and platelet function (Fig. S3 B), indicating biological relevance.

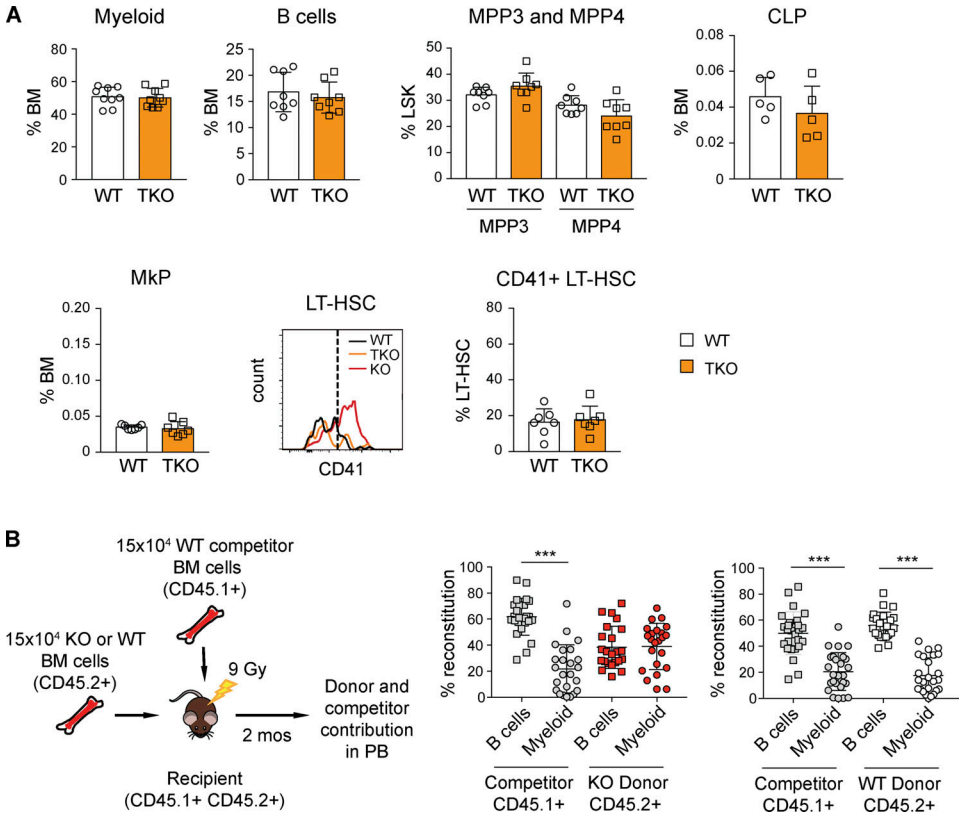

Figure 5. **HSPC phenotype in TKO mice and competitive repopulation assays. (A)** Analysis of the indicated populations in mice with a Helios deletion in T cells. WT, Ikzf2$^{f/f}$ CD4-Cre^{-}; TKO, Ikzf2$^{f/f}$ CD4-Cre^{+}; KO, Ikzf2$^{-/-}$. Sex- and age-matched (10–20-wk-old) mice were studied. Mean ± SD of five to eight independent experiments. **(B)** Strategy of competitive BM transplantations (left). PB, peripheral blood. The percentage of B and myeloid cells from competitor and donor cells is indicated. Mean ± SD of four independent experiments with six or seven recipient mice per genotype. Unpaired two-tailed *t* test: ***, P < 0.001.

KO LT-HSCs resembled HSCs of old mice, as they up-regulated age-associated genes related to megakaryopoiesis and non-Mk-associated processes like *Gprc5c* and *Fzd1* (Fig. 6 B and Table S1). In a complementary experiment, we analyzed the transcriptomes of WT and KO CD34^{-}Flt3^{-} LT-HSCs and lymphoid-primed L-MPPs (CD34^{+}Flt3^{+} LSK) by microarray (Fig. S3, C and D). CD34^{-} LT-HSCs exhibited the most gene expression changes between KO and WT, with a strong enrichment of MkP and aging HSC signatures in the KO, similar to CD150^{+}CD48^{-} HSCs, and a decrease of the CLP signature in the KO L-MPP samples.

The similarity between KO LT-HSCs and aging HSCs suggested that Helios levels may diminish with age. We compared Helios expression in LT-HSC, ST-HSC, and MPP populations of young (10-wk-old) versus old (>1-yr-old) WT mice (Fig. S3 E). Indeed, Helios proteins were expressed at lower levels in the LT-HSCs of old mice compared with young, while the ST-HSCs and MPPs showed similar Helios levels between young and old animals. Helios was similarly decreased in both the CD41^{+} and CD41^{-} LT-HSC subsets of old mice compared with the equivalent populations in young animals (Fig. S3 F). These results suggested that the increase in megakaryopoiesis, and decrease in lymphopoiesis, in old animals is in part be due to a reduction in Helios levels.

To determine if the aging signature in the KO transcriptomes reflected bona fide HSPC aging, we compared these cells in young (10–12 wk of age) versus old (>1 yr of age) WT and KO animals (Fig. 6 E). If the HSPCs of young KO mice were "old," then their frequencies should be similar to those of old mice. Furthermore, the differences between WT and KO HSPCs of young animals should be diminished between WT and KO cells of old mice, as the HSPCs of old WT animals would "catch up" with those of old KO mice. This did not happen. The frequencies of CD41^{+} LT-HSCs, CD41^{+} MPP2, and MkP populations increased between young KO and old KO mice, while those of MPP4 cells fell, and the differences between WT and KO remained significant in both young and old animals. In addition, old KO BM did not exhibit more pathological signs compared with WT. Thus Helios deficiency is associated with aging features that appear early and are exacerbated in old mice.

Collectively, these results indicated that Helios-deficient HSPCs up-regulate a megakaryocyte and aging gene expression signature and down-regulate a lymphoid gene expression program.

Helios transcriptionally represses megakaryocyte gene expression

To find Helios target genes, we investigated its genomic binding sites in hematopoietic precursor cells, by chromatin immunoprecipitation sequencing (ChIP-seq), using the hematopoietic precursor cell line HPC7 (Pinto do O et al., 1998), as we could not

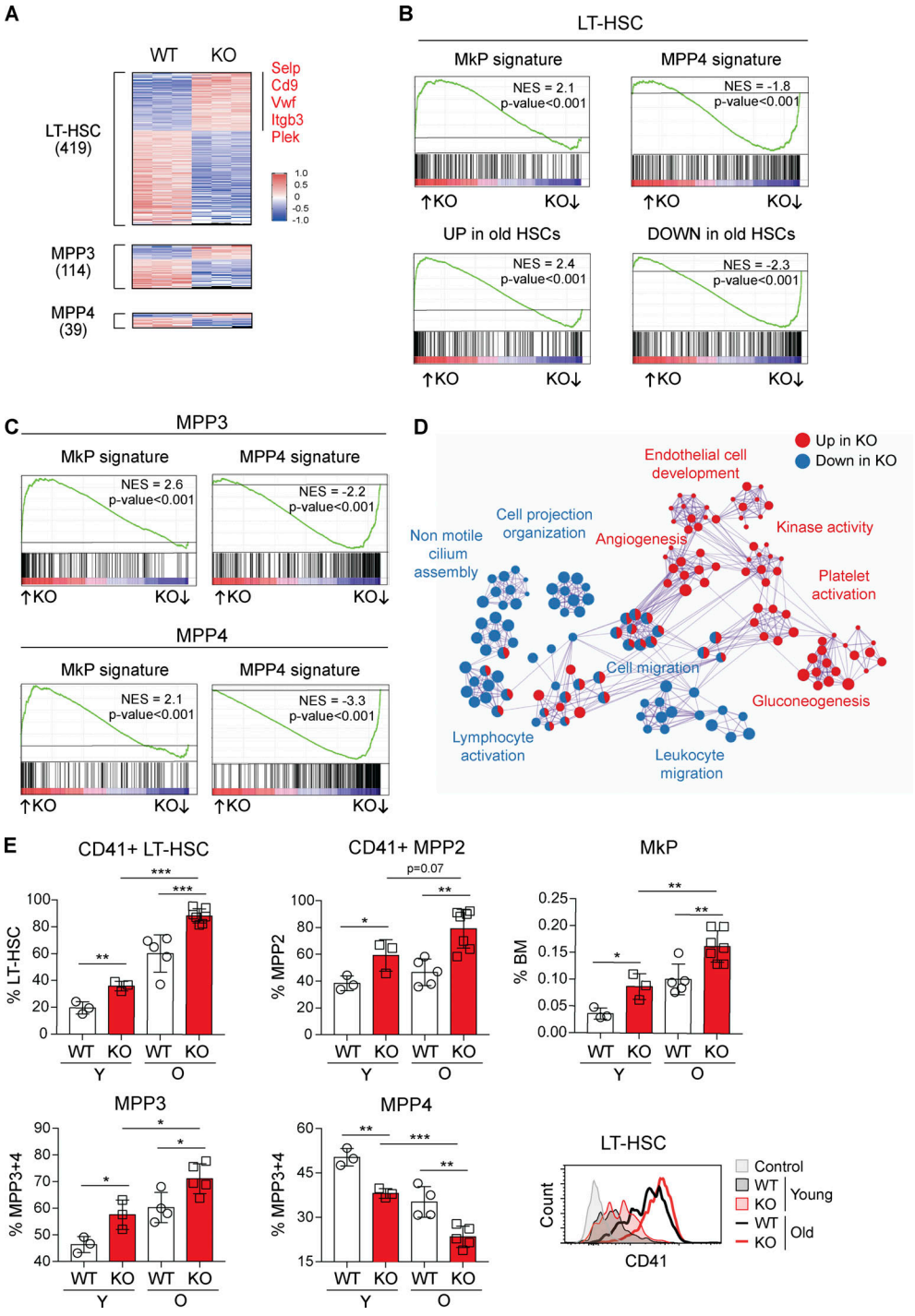

Figure 6. **Helios KO HSPCs are transcriptionally primed toward the megakaryocyte lineage. (A)** Heatmap of up- and down-regulated genes in LT-HSCs, MPP3 cells, and MPP4 cells. Highlighted genes in the LT-HSC samples correspond to those specific for MkPs and up-regulated (in red). **(B and C)** GSEA of the indicated populations. Ranked gene lists comprise all genes detected in the RNA-seq analysis, ranked according to their FC (KO vs. WT). Gene sets correspond to signature genes for MkPs (Grover et al., 2016), MPP4s (described in Materials and methods), and genes up- or down-regulated in old LT-HSCs (Sun et al., 2014). The normalized enrichment score (NES) and P values are shown for each analysis. **(D)** Metascape analyses of up- (red) and down- (blue) regulated genes in the KO LT-HSCs. Each cluster is defined by its identity name and is composed of nodes that share similar genes. Node size is proportional to the gene content number. **(E)** Relative abundance of the indicated BM populations in young (15-wk-old) and old (>1-yr-old) WT and KO mice. The histogram shows representative levels of CD41 in WT and KO LT-HSCs from young and old mice. Mean ± SD of five independent experiments, with three to seven mice per genotype. Unpaired two-tailed *t* test: *, P < 0.05; **, P < 0.01; ***, P < 0.001.

purify enough primary LSK cells for these experiments. HPC7 cells express Helios and comprise a mix of cells with LSK and LK features (Fig. S4 A), which differentiate into multiple hematopoietic lineages in the presence of appropriate cytokines and retain multipotency in vivo (Pinto do O et al., 1998; Chen et al., 2019). Our results revealed 15,709 Helios-bound peaks that mapped near 8,739 genes; binding was observed at gene bodies, distal regions, and proximal promoters (Fig. S4 B). Motif enrichment analysis identified GGAA-containing motifs as highly enriched at Helios-bound peaks (Fig. S4 C), as expected for an Ikaros family member. Moderate but significant enrichment over background was detected at genes deregulated in Helios KO LT-HSCs (50.3% [red bar] vs. 40.7% [gray bar]; Fig. S4 D), indicating both direct and indirect regulation by Helios. Similar enrichments were also seen at genes deregulated in MPP3 and MPP4 cells, but they were not significant due to the low number of deregulated genes in these populations (not shown). We also asked if Helios binding was enriched at genes defining the signatures of specific HSPC populations. Interestingly, Helios binding was enriched at MPP4- and MkP-specific, but not LT-HSC–specific, genes (Fig. S4 D, orange bars). Thus, Helios may directly regulate genes involved in lineage specification, but not stemness, in HSPCs.

We then evaluated the effect of Helios binding on chromatin accessibility, by integrating the HPC7 ChIP-seq data with an analysis of accessible chromatin between WT and Helios KO LSK cells by assay for transposase-accessible chromatin using sequencing (ATAC-seq). This showed that Helios does not modify the location or relative number of accessible regions, as the >130 × 10^3 regions were mostly shared between WT and KO DNA. In all, 10,890 regions bound by Helios ("Helios sites") overlapped with ATAC-seq peaks. Helios binding markedly coincided with chromatin closing in WT cells, with a clear bias toward increased accessibility in the KO chromatin (Fig. 7 A, all ATAC peaks). We evaluated the importance of Helios sites at regions where the ATAC-seq peaks were strongly (log2 fold change [log2FC] >0.3) or weakly (log2FC <0.3) affected in the KO cells and compared those that became more open (red) or more closed (black; Fig. 7 B). Helios sites were selectively enriched in the regions that were more open in the KO cells, especially those with the biggest increases in accessibility (among all ATAC-seq peaks). Importantly, the frequency of Helios binding was strongly and significantly increased when ATAC-seq regions were filtered for those with the most significant increases in chromatin opening (Fig. 7 B, right). While both MkP and MPP4 genes contained Helios sites that correlated with chromatin opening (Fig. 7 A), more MkP target genes became more open without Helios compared with MPP4 targets or random genes (Figs. 7 C and S4 E). These included genes important for megakaryocyte differentiation (*Itgb3* and *Itga2b*, which encode CD61 and CD41, *Runx1*, and *Mpl*; Fig. 7, C and D) and function ("response to wounding"; Fig. S4 F). In contrast, critical MPP4 genes (*Flt3*, *Ccr7*, and *Irf8*) exhibited minimal change in the KO chromatin (Fig. S4 G), and lymphoid-related terms were not found for genes with decreased or increased chromatin accessibility (not shown). These results suggested that Helios is primarily involved in chromatin compaction in the genes required for megakaryocyte differentiation.

Interestingly, Helios sites were enriched for Gata2 and Runx1 motifs (Fig. 7 E). Since the Gata2 and Runx1 binding profiles were previously mapped in HPC7 cells (Wilson et al., 2010), we integrated these data with our Helios ChIP-seq and ATAC-seq results. The Helios sites that were also bound by Gata2 or Runx1 were markedly associated with increased accessibility gains in KO cells when compared with Helios sites that were not (Fig. 7 F; and Fig. S4, H and I). Further, the Helios sites that became more closed were depleted of Gata2 and Runx1 binding (Fig. S4 I). Since Gata2 and Runx1 have been shown to promote megakaryocyte commitment and differentiation (Ichikawa et al., 2004; Pencovich et al., 2011; Pimkin et al., 2014; Pulecio et al., 2016; Estevez et al., 2021), we asked if at the target sites shared by Helios, Gata2 and Runx1 were enriched at MkP genes. This turned out to be the case, compared with random or MPP4 genes (Fig. 7 G). The MkP bias was even more pronounced when only the Helios sites that were more open in the KO were considered (log2FC >0.2). The top pathway enriched for genes bound by all three factors was response to wounding (Figs. 7 H and S4 H, cluster C1), suggesting that Helios limits chromatin accessibility at Gata2 and Runx1 targets important for megakaryopoiesis and function.

Thus, Helios promotes widespread chromatin compaction at target genes important for HSPC commitment toward the platelet lineage, with potentially negative consequences for megakaryocyte lineage priming by Gata2 and Runx1.

Helios impacts the appearance of megakaryocyte- and lymphoid-biased HSPCs

To determine how Helios loss affects the gene expression program of lineage-primed HSPCs at the single-cell level, we analyzed WT and KO LSK cells by single-cell RNA-seq. Purified LSK cells from 10-wk-old animals were stained with anti-CD150 and anti-CD48 oligo-tagged antibodies (Abs) to track HSCs and MPP cells (cellular indexing of transcriptomes and epitopes by sequencing [CITE-seq]) and labeled with Hash-Tag-Oligo (HTO)–conjugated anti-CD45 and anti-MHC class I Abs to identify the mouse of origin (Stoeckius et al., 2017, 2018). 2,500 cells from each sample were pooled and subjected to 10X Genomics library preparation, which allowed the mRNA from single cells and their associated Ab-oligos to be tagged with a unique index. After library sequencing and further quality control filtering, these experiments allowed us to analyze the mRNA profiles of 3,470 unique cells out of the starting 10^4.

To visualize the HSPC compartment, we generated 2D maps using the Uniform Manifold Approximation and Projection (UMAP) tool and evaluated the characteristics that assigned each cell to a particular area. Principal-component analysis (PCA) was used to dissect the gene expression signatures, and principal components 1, 2, and 3 (PC1–PC3) captured the biggest differences between the cells (Fig. S5 A). PC1 and PC2 were mainly defined by genes related to the cell cycle (Fig. S5, B–D) and included those implicated in DNA replication (PC1-negative), mitosis (PC2-negative), ribosome biogenesis, and DNA integrity checkpoint (PC2-positive). The HSPCs identified by their PC1 and PC2 coordinates were therefore separated according to their proliferative status along the vertical axis of the UMAP plot;

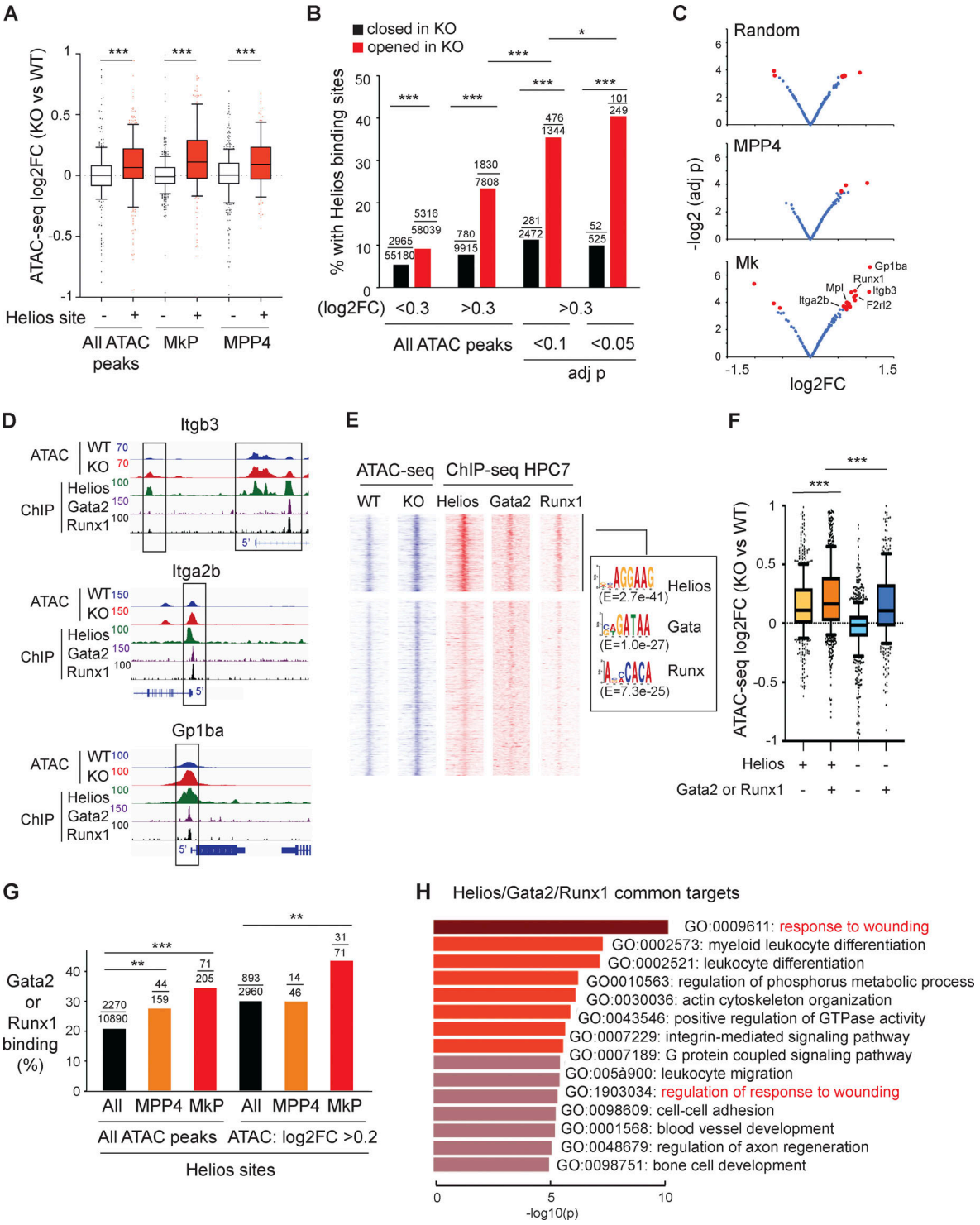

Figure 7. **Helios targets HSPC genes through gene repression. (A)** Box plots showing the distribution of the log2FC values of the ATAC-seq peaks in KO versus WT LSK samples, bound or not by Helios in HPC7 cells, either among all ATAC-seq peaks or those associated with MPP4 and MkP signature genes. Each box plot was generated with a random selection of 300 regions. Mann–Whitney test: ***, P < 0.001. **(B)** Percentage of chromatin regions containing "Helios sites" where the ATAC-seq peaks varied between WT and KO cells. Left: ATAC-seq peaks were divided into four subsets, based on whether their intensity decreased or increased < or >0.3-fold (log2FC) in KO cells. Right: Percentage of Helios binding at ATAC-seq peaks with the most significant variations (FC >0.3, adj P < 0.1 or adj P < 0.05). The numbers above each bar indicate the number of Helios-bound peaks (top) within the total number of peaks in the subset (bottom). Hypergeometric test: *, P < 0.02; ***, P < 10^{-10}. **(C)** Volcano plots showing log2FC versus –log2(adj p) for Helios-bound MkP and MPP4 genes or a set of random genes. Red dots highlight regions for which –log2(adj p) was >3.5. **(D)** Integrative genome viewer screenshots of representative platelet genes. Shown are ATAC-seq signals in WT and KO LSK cells and Helios, Gata2, and Runx1 binding in HPC7 cells (Gata2 and Runx1 data are from the GEO dataset GSE22178). Boxed regions belong to the regions selected in C as having significant increases of ATAC-seq signals in KO cells. **(E)** Seq-miner heatmap showing 4,370 regions with significantly increased ATAC-seq signals in KO versus WT LSK cells (adj P < 0.2), along with Helios, Gata2, and Runx1 binding in HPC7 cells.

Motif enrichment within the 1327 ATAC-seq peaks bound by Helios (top cluster). **(F)** Box plot showing ATAC-seq log2FC for regions bound or not by Helios and/or Runx1 and Gata2. ***, P < 0.001 (Mann–Whitney test). **(G)** Frequency of Gata2 and/or Runx1 binding on Helios-bound MPP4 and MkP sites. In the right part of the graph, analyzed regions were restricted to those with an ATAC-seq log2FC >0.2. **, P < 0.01; ***, P < 0.001 (hypergeometric test). **(H)** Metascape analysis of the enriched pathways associated with genes commonly bound by Helios and/or Gata2 and Runx1 (cluster C1 in Fig. S4 H). Pathways associated with the megakaryocyte lineage are highlighted.

quiescent cells (blue) were found at the top, while cells at early (orange) and late (green) stages of the cell cycle were clustered at the bottom (Fig. 8 A).

PC3 genes were associated with lineage priming (Fig. 8 B; and Fig. S5, B and E). The cells identified by negative PC3 values expressed high mRNA levels for genes associated with HSCs and MPP2 cells (e.g., *Mpl*, *Gata2*, and *Cd9*) according to our RNA-seq data and the ImmGen datasets (MPP2). These cells clustered to the left of the UMAP plot (Figs. 8 B and S5 E). In contrast, the cells identified by positive PC3 values expressed abundant transcripts for genes characteristic of lymphoid-primed MPP4 cells (e.g., *Flt3*, *Dntt*, and *Cd53*), and they clustered to the right. The cells in the middle expressed PC3 genes at intermediate levels compared with HSC/MPP2 and MPP4 cells and probably corresponded to MPP3 cells (Fig. S5 E), suggesting that myeloid-biased MPPs express genes associated with both megakaryocytes and lymphocytes. Similar results were obtained when we compared the cells expressing CD150 (encoded by the *Slamf1* gene) and CD48 at the mRNA and protein levels (Fig. S5 F): $CD150^+CD48^-$ cells were located to the left (as were $Slamf1^+Cd48^-$ and $Cd34^-Cd48^-$ cells), and $CD150^-CD48^+$ (and $Slamf1^-Cd48^+$) cells (which included MPP3 and MPP4 cells) were mapped to the center and the right. Approximately 500 cells in the dataset corresponded to HSC/MPP2 cells, as defined by their Mpl^+Flt3^- (n = 468; Fig. 8 B) or $CD150^+CD48^-$ (n = 596; Fig. S5 F) phenotypes.

These analyses revealed that the Helios KO LSK population contained strikingly more HSC/MPP2 ($Flt3^-Mpl^+$) cells than WT (Fig. 8 B), indicating that the megakaryocyte gene expression signature is already firmly established in HSPCs. Interestingly, the opposite was true for MPP4 ($Flt3^+Mpl^-$) cells, which were robustly represented in WT HSPCs, but not in KO. This suggested that HSPCs shift toward megakaryocyte commitment in the absence of Helios. To quantify the number of cells that were megakaryocyte biased and determine their cell cycle state, we generated heatmaps of WT and KO quiescent and cycling cells using the top 30 PC3-negative and -positive genes and ranked the cells according to their PC3 coordinates (Fig. 8, C and D, left). A "priming score" was calculated for every cell, based on the number of expressed HSC/MPP2 (counted as −1 per gene) and MPP4 (+1 per gene) genes. Cells that expressed a predominantly HSC/MPP2 gene expression signature had an overall negative score, while those that expressed an MPP4 signature had an overall positive score. This showed that Helios KO HSPCs were highly enriched for megakaryocyte-primed cells, particularly among quiescent cells (Fig. 8, C and D, right), a result that is consistent with our bulk RNA-seq analysis, which revealed that LT-HSCs, mostly quiescent, are more deregulated in the absence of Helios than the more proliferative MPPs, and suggests that Helios negatively regulates megakaryocyte priming as early as the quiescent stem cell stage.

Altogether, our results indicate that Helios limits the output of megakaryocyte-biased MPPs from the quiescent HSPC population by transcriptionally repressing the megakaryocyte gene expression program normally activated by Gata2 and Runx1 during megakaryocyte priming.

Discussion

Here, we uncover a key role for Helios as an inhibitor of megakaryocyte priming in HSPCs. We show that Helios acts as a transcriptional repressor of the megakaryocyte gene expression program and promotes chromatin compaction at these targets, which likely antagonizes the megakaryocyte-priming activities of Gata2 and Runx1 in HSCs. On the other hand, Helios positively regulates the gene expression programs implicated in cell migration and mechanotransduction. These mechanisms explain why hematopoiesis is so strongly skewed toward the megakaryocyte lineage in Helios-null mice. Our results support a model in which negative priming events are as important as positive ones for maintaining HSPC pluripotency.

Lymphoid commitment is also strongly reduced in Helios KO animals. Our results suggest that in the absence of events that restrict lineage priming, megakaryopoiesis dominates hematopoietic development at the expense of lymphopoiesis. Our data support the concept that P-MPP and L-MPP restriction occur at opposite ends of the commitment process. P-MPPs separate first, and the number of HSPCs that can be biased toward this lineage is continuously blocked by Helios. By limiting P-MPP separation, and perhaps additional events, Helios maintains the pluripotency of the HSPC pool for further lineage restriction and contributes to the developmental antagonism between the megakaryocyte and lymphoid lineage programs. Interestingly, even phenotypic MPP4 cells from Helios KO mice are not efficiently committed to the lymphoid lineage, as indicated by their enhanced MkP gene expression program, diminished MPP4 and CLP signatures, and reduced ability to become B cells following transplantation. This suggests that Helios affects lineage commitment beyond the HSC stage, perhaps by promoting MPP4 migration toward IL-7–rich perisinusoidal areas of the bone that are important for lymphoid priming (Aurrand-Lions and Mancini, 2018).

At genes that gain accessibility in the Helios-null HSPCs, there is a significant overlap between Helios-binding sites and those bound by Gata2 and Runx1, two major transcriptional activators of the megakaryocyte program. Helios may therefore antagonize Gata2 and Runx1 function at the enhancer regions of common target genes. Interestingly, Gata2 and Runx1 sites also overlap with Ets factor motifs (Doré et al., 2012), and Ets proteins have been reported to promote megakaryopoiesis (Tijssen and Ghevaert, 2013). Since Ikaros family proteins and Ets factors both bind sequences containing GGAA (Trinh et al., 2001),

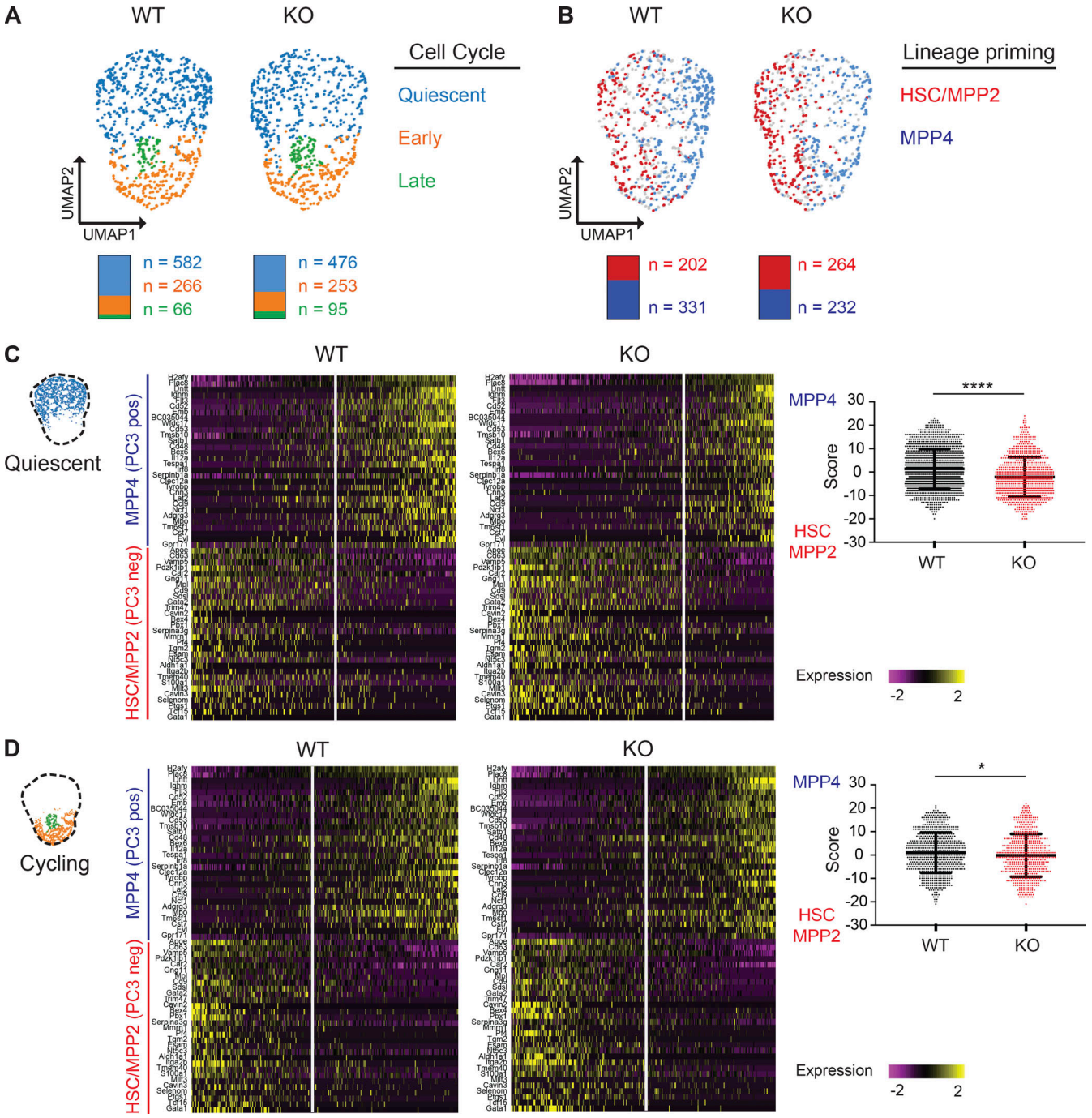

Figure 8. **Helios affects lineage priming at the single-cell level. (A and B)** UMAP plots of WT and KO HSPCs, derived from one WT and one KO sample with similar numbers of sequenced cells. **(A)** Characterization and quantification of HSPCs based on their cell cycle feature, as indicated. **(B)** Characterization and quantification of HSPCs based on their lineage-priming features. The quantification of the cells is shown below the UMAP plots. **(C)** Left: Heatmaps of single, quiescent WT and KO HSPCs. The order of the cells from left to right corresponds to their lineage priming score. The y axis indicates the 60 genes that contribute the most to the PC3 variance (top 30 negative genes in red, and top 30 positive genes in blue). The white vertical lines correspond to the positions of cells with a lineage priming score of 0. Right: Lineage-priming score of WT and KO quiescent HSPCs. Mean ± SD of two pooled independent experiments. **(D)** Left: Heatmaps of single, cycling WT and KO HSPCs, ordered as in C. Right: Lineage-priming score of WT and KO cycling HSPCs. Mean ± SD of two pooled independent experiments. Statistical significance calculated with Mann–Whitney test: *, P = 0.01; ****, P < 0.0001.

Helios may also antagonize Ets protein binding and function at megakaryocyte genes.

How Helios promotes chromatin compaction in HSPCs remains to be determined. Helios has been shown to mediate the recruitment of the nucleosome remodeling and deacetylase (NuRD) complex to chromatin (Sridharan and Smale, 2007), and the Helios homologue Ikaros can recruit NuRD to trigger nucleosome deposition and chromatin compaction at a target gene

(Liang et al., 2017). We previously showed that Ikaros also recruits Polycomb repressive complex 2 to deposit the repressive epigenetic mark H3K27me3 at certain target genes in thymocytes, including the megakaryocyte genes *Cd9* and *Vwf* (Oravecz et al., 2015). Thus, Helios may prevent megakaryocyte priming through a combination of partner complexes depending on the target gene.

B and T cell development are differentially affected by Helios deficiency. We show that MPP4s, CLPs, and immature B cells are decreased in Helios KO mice and that mutant B, but not T, cells are reduced after LT-HSC transplantation compared with WT. These results suggest that B cell commitment is more sensitive to Helios and are reminiscent of earlier studies that showed that CLPs, biased toward B cells, are more sensitive than early T lineage progenitors to the loss of Ikaros (Allman et al., 2003). Helios may thus cooperate with Ikaros to promote CLP development. Moreover, thymus-resident progenitors can self-renew in the absence of incoming BM-derived progenitors, providing an additional layer of support for T cell development (Martins et al., 2014).

Recently, Helios was reported to promote leukemic stem cell renewal during acute myeloid leukemia progression (Park et al., 2019). It is unclear how the physiological function of Helios relates to its oncogenic activity, but we noted that genes related to "acute myeloid leukemia" were enriched among those with increased accessibility in the KO cells (Fig. S4 F), suggesting a possible link. Curiously, the authors concluded that Helios was dispensable for early hematopoiesis. However, their analyses focused on populations in which we also did not see differences (LSK, LK, GMP, CMP, and MEP of young mice), and the effects of Helios on HSCs and MPPs were not closely studied. Our two studies also used different experimental approaches (e.g., non-competitive vs. the competitive repopulation assays studied here and tissue-specific vs. germline KO mouse models, though the mutations are similar). Therefore, it is likely that the present phenotype was previously missed because of a difference in protocol, even though we cannot exclude that the HSC-specific *Ikzf2* deletion may lead to milder phenotypes.

Among Ikaros family members, Helios and Ikaros are highly expressed in HSPCs, where they appear to perform both unique and redundant functions. Ikaros was previously found to be essential for HSC maintenance and/or survival (Nichogiannopoulou et al., 1999), a function that is not shared by Helios. On the other hand, both Helios (shown here) and Ikaros positively affect lymphoid priming (Ng et al., 2009). We showed here that Helios is required to limit megakaryocyte priming within quiescent LT-HSCs. Interestingly, Ikaros also represses megakaryocyte-associated gene expression (Yoshida et al., 2006; Malinge et al., 2013; Liu et al., 2018). In particular, a recent study of myelodysplastic syndrome patients reported that lenalidomide treatment, which degrades Ikaros family proteins in human cells, results in megakaryocyte differentiation of the transformed cells via Gata and Runx1 activation (Martinez-Høyer et al., 2020), a finding that echoes our results here. How Ikaros regulates megakaryocyte gene expression in HSCs remains unknown. It will thus be important to determine if Ikaros and Helios cooperate at target genes, perhaps as heterodimers, to repress megakaryocyte commitment.

In conclusion, our study sheds light on the significance of negative priming events in HSPCs. It will be important to understand if multiple factors work in tandem to block lineage commitment and how widespread the antagonistic mechanism is between negative and positive regulators for other hematopoietic lineages.

Materials and methods

Mice

Helios germline (Ikzf2$^{-/-}$, KO), Helios floxed (Ikzf2$^{f/f}$), Rosa-CreERT2, and CD4-Cre transgenic mice were previously described (Cai et al., 2009; Sebastian et al., 2016; Badea et al., 2009; Wolfer et al., 2001). Helios KO mice were backcrossed six generations onto the C57BL/6 background, while Ikzf2$^{f/f}$, Rosa-CreERT2, and CD4-Cre mice were backcrossed >10 generations. To delete the Ikzf2$^{f/f}$ allele, mice were injected intraperitoneally with tamoxifen (75 mg/kg T568; Sigma-Aldrich) in sunflower oil every day for 5 d and analyzed 3 wk after the first injection. To induce a stress response, mice were intraperitoneally injected with a single dose of high molecular weight poly I:C (5 mg/kg; Invivogen) or saline (NaCl 0.9%) and analyzed 16 h later. All mice were bred and maintained in a specific pathogen–free facility and used according to IGBMC Ethical Committee guidelines. Animal experiments were approved by the ethical section of the French Ministry of Research and Innovation with the approval number APAFIS 14189–201803211054329. Both female and male mice were investigated and evenly distributed in the different experimental groups; aged-matched animals were studied.

Flow cytometry and cell sorting

Cells were stained with the Ab combinations listed in Table S2 in PBS/0.5% BSA/2 mM EDTA. Samples were acquired on a LSR II or Fortessa analyzer (BD Biosciences) and analyzed with FlowJo10 software. For intracellular staining, cells were fixed overnight (ON) at 4°C and then permeabilized and stained with the primary Ab for 1 h at room temperature and, when necessary, with a secondary Ab for 1 h on ice using the eBioscience Foxp3/Transcription Factor Staining Kit (Thermofisher). For cytokine staining, CD4$^+$ T cells were first magnetically enriched using the Dynabeads Untouched Mouse CD4 Cells Kit (Thermofisher) and then stimulated for 2 h at 37°C with PMA and ionomycin (0.5 µg/ml each) in the presence of BD GolgiPlug (BD Biosciences) in IMDM supplemented with 10% FCS, MEM, Hepes (10 mM), GlutaMAX (Gibco), sodium pyruvate (1 mM), and 2-mercaptoethanol (50 µM). Cells were stained and analyzed as above. For sorting HSPC subsets, cells were stained for lineage marker expression (Table S2) before depletion with Dynabeads sheep anti-rat IgG beads (Thermofisher). Lineage-negative cells were stained as above and sorted in the presence of DAPI (1 µM/ml) using a FACS ARIA II or Fusion (BD Biosciences). Sort purity was >98%.

CFU assays

For CFU-Mk and CFU-Myeloid assays, 50 × 10^3 cells were cultured in methylcellulose media (MethoCult 3231; Stemcell Technologies) in the presence of recombinant mouse (m) SCF

(50 ng/ml), mTPO (50 ng/ml), human (h) EPO (5 U/ml), mIL-3 (20 ng/ml) and mIL-11 (40 ng/ml; cytokines from PeproTech), as described previously (Akashi et al., 2000). For CFU-preB assays, 15 × 10^4 cells were cultured in methylcellulose media containing hIL-7 (MethoCult 3630; Stem Cell Technologies). All assays were performed in duplicate, and CFUs were counted after 7 d. Single colonies were cytospun onto slides, subjected to May-Grünwald-Giemsa (MGG) staining, and analyzed with an upright microscope (DM4000 B 40X; Leica). Images were captured with the Coolsnap software.

HSPC single-cell cultures

For LT-HSCs ($CD48^-CD150^+$ LSK), single cells were sorted and cultured in U-shaped 96-well plates containing 50 µl StemSpan SFEM (Stemcell Technologies) supplemented with 10% FCS, 2-mercaptoethanol (50 µM), penicillin/streptomycin, mIL-3 (20 ng/ml), mSCF (50 ng/ml), and mTPO (50 ng/ml; cytokines from PeproTech; Sanjuan-Pla et al., 2013). CFUs were evaluated at day 10. For MPPs ($CD48^+CD150^-$ LSK), single cells were sorted and cultured in flat-bottom 96-well plates in 50 µl complete methylcellulose media (MethoCult 3434; Stemcell Technologies). CFUs and morphology were evaluated after 7 d. Single colonies were cytospun and stained as above.

BM competitive transplantation assays

15 × 10^4 WT or KO BM cells from 10–15-wk-old $CD45.2^+$ mice were i.v. injected with 15 × 10^4 $CD45.1^+$ WT BM cells into 9-Gy lethally irradiated $CD45.1^+CD45.2^+$ hosts. Peripheral blood was analyzed 2 and 4 mo after reconstitution, as described previously (Mastio et al., 2018). The contributions to myeloid ($CD11b^+B220^-$), B ($CD11b^-B220^+$), and T cells ($CD11b^-B220^-CD4^+CD8^+$) from donor or competitor origin were defined respectively as the percentage of cells within the $CD45.2^+Ter119^-$ or $CD45.1^+Ter119^-$ populations.

LT-HSC repopulation assays

100 WT or KO LT-HSCs ($CD48^-CD150^+$ LSK) from 6-wk-old $CD45.2^+$ mice were i.v. injected with 5 × 10^5 supporting $CD45.1^+$ WT BM cells into 9-Gy lethally irradiated $CD45.1^+CD45.2^+$ hosts. Peripheral blood was analyzed 2 and 4 mo after transplantation. The contributions to donor myeloid ($CD11b^+B220^-$), B ($CD11b^-B220^+$), and T cells ($CD11b^-B220^-CD4^+CD8^+$) were defined as the percentage of cells within the $CD45.2^+Ter119^-$ population.

MPP3 and MPP4 potential in vivo assays

5 × 10^3 WT or KO MPP3 ($CD48^+CD150^-Flt3^-$ LSK) or MPP4 ($CD48^+CD150^-Flt3^+$ LSK) cells from 15-wk-old $CD45.2^+$ mice were i.v. injected into 6-Gy sublethally irradiated $CD45.1^+CD45.2^+$ hosts. Peripheral blood was analyzed 2 wk after transplantation. Mice with <0.5% $CD45.2^+$ cells were excluded from the analysis (in total, 4/60 mice were excluded). The percentage of $CD45.2^+$ myeloid ($CD11b^+B220^-$) and B ($CD11b^-B220^+$) cells was analyzed.

Transcriptome analysis by microarray and GSEA

The transcriptomes of 5 × 10^3 LT-HSCs ($CD34^-Flt3^-$ LSK) and 5 × 10^4 L-MPPs ($CD34^+Flt3^+$ LSK) from WT and KO 6-wk-old mice (three each) were analyzed with Affymetrix 430.2.0 arrays. RNA was extracted with the RNeasy Micro kit (Qiagen), and biotinylated cRNA targets were prepared, starting from 2 to 20 ng total RNA, using the Message Amp II aRNA Amplification Kit (Ambion) with two rounds of amplification, according to manufacturer's recommendations. cRNAs were hybridized to the microarrays using standard conditions. Hierarchical clustering was performed using Cluster 3 software. GSEA was performed using the GSEA 2.0 software (Subramanian et al., 2005). In these experiments only, the mice came from a mixed C57BL/6 and 129/Sv genetic background.

Transcriptome analysis by RNA-seq

Total RNA was extracted from 1 to 4 × 10^4 LT-HSCs ($CD48^-CD150^+$ LSK), MPP3 cells ($CD48^+$ $CD150^-Flt3^-$ LSK), and MPP4 cells ($CD48^+CD150^-Flt3^-$ LSK) from WT and KO 10-wk-old mice (three each) using the RNeasy Plus Micro Kit (Qiagen). Libraries were prepared with the Clontech SMART-seq v4 Ultra Low Input RNA Kit for Sequencing, followed by the Illumina Nextera XT DNA library preparation kit, and sequenced with a HiSeq 4000 (Illumina) with single-end 50-bp read length. Reads were preprocessed to remove adapters using Cutadapt version 1.10, poly(A) and low-quality sequences (Phred quality score <20). Reads shorter than 40 bases were discarded and then aligned to the *Mus musculus* genome mm10 using STAR v2.5.3a. Gene expression quantification was performed from uniquely aligned reads using HTSeq (v0.6.1p1), with annotations from ENSEMBL GRCm38 and "union" mode. Differential gene expression analyses were performed using the Bioconductor package DESeq2 (v1.16.1) on R (v3.3.2). FC rank ordering statistics was used to compute f-values (Dembélé and Kastner, 2014), which correspond to a method based on ranks of the FCs of all pairwise comparisons. Differentially expressed genes were selected according to the following criteria: (1) adj P < 0.20, (2) f-value <0.02 or >0.98, and (3) normalized reads per kilobase >20 for all samples in either the WT or KO group. Heatmaps of differentially expressed genes were created using Cluster and Java TreeView software. For the GSEA, the KO versus WT FCs of all genes detected in the RNA-seq experiments were used for the ranked genes lists. The MPP4 signature was obtained using our transcriptome data. MPP4 signature genes were identified as the genes with significant differential expression (adj P < 0.05, log2FC >1) in both the WT LT-HSC versus WT MPP4 and WT MPP3 versus WT MPP4 comparisons. The CLP, MkP, and old HSC signatures were taken from the literature (Drissen et al., 2016; Sun et al., 2014). Pathway analyses were performed at the Metascape website (http://metascape.org; Zhou et al., 2019).

Single-cell mRNA-seq

3.5 × 10^4 LSK cells from WT and KO 10-wk-old mice (two each) were individually labeled with unique oligonucleotide-tagged Abs against CD45 and MHC class I (TotalSeq Hash-tag 1 #A0301, Hash-tag 2 #A0302, Hash-tag 3 #A0303, Hash-tag 4 #A0304; BioLegend) in order to multiplex the four samples (Anders et al., 2015). Each LSK sample was then labeled with anti-CD150 and anti-CD48 Abs conjugated with an oligonucleotide containing a unique barcode for Ab identification (TotalSeq anti-CD150 #115945, anti-CD48 #103477; BioLegend; Stoeckius et al., 2017, 2018). After Hash-tagged and CITE-tagged cells

were counted and checked for viability, 10^4 cells (2,500 LSK cells from each sample) were loaded into a Chromium Controller (10x Genomics), captured and library prepared with the Chromium Single Cell 3′ v2 Kit (10x Genomics). Briefly, following cell lysis inside droplets, cellular mRNA and Ab-derived oligos were reverse transcribed and indexed with a shared cellular barcode. Indexed cDNAs were pooled and amplified by PCR according to the Chromium Single Cell 3′ v2 protocol with specific primers to amplify the Ab tags. SPRI bead size selection was performed to separate the mRNA-derived cDNA (>300 bp) and the Ab-derived tagged cDNAs (180 bp). For the mRNA-derived cDNA library preparation, we followed the manufacturer's instructions for Single Cell 3′ v2 protocol. For Ab-derived tagged libraries, we used the KAPA HiFi HotStart Library Amplification Kit (Roche) with the following primers and amplification program.

CITE-seq (antibody-derived tag [ADT]) library

Amplification was performed at 95°C for 3 min followed by 10 cycles at 95°C for 20 s, 60°C for 30 s, 72°C for 20 s, and elongation at 72°C for 5 min with the 5′-CAAGCAGAAGACGGCATACGAGATCGTGATGTGACTGGAGTTCCTTGGCACCCGAGAATTCCA-3′ small RNA RPI1 primer as the i7 primer (Illumina).

Hash-tag-seq (HTO) library

Amplification was performed at 95°C for 3 min followed by 10 cycles at 95°C for 20 s 64°C for 30 s, 72°C for 20 s, and elongation at 72°C for 5 min with the 5′-CAAGCAGAAGACGGCATACGAGATCGAGTAATGTGACTGGAGTTCAGACGTGTGC-3′ TruSeq D701_s primer as the i7 primer (Illumina).

The 5′-AATGATACGGCGACCACCGAGATCTACACTCTTTCCCTACACGACGCTC-3′ primer was used as the i5 primer (Illumina) for both CITE- and HASH-seq library amplification.

Following final bead purification, all three libraries were pooled as 80% mRNA library, 10% ADT library, and 10% HTO library before sequencing. cDNA libraries were sequenced on the HiSeq 4000 paired-end 100bp read length.

Gene expression and library analyses

The 3′ mRNA-seq library reads were processed using CellRanger pipeline v3.0.2 on mm10 and ENSEMBL GRCm38. Cell hashing- and CITE-seq–derived library reads were merged together and processed with 3′ mRNA-seq library using the Feature Barcoding Analysis option. Tag identification from the HTO library was performed using the approach proposed by the Seurat R package v3.0.0 and R v3.5.1 on HTO counts (Butler et al., 2018; Stoeckius et al., 2018). Further, the CellRanger count was used to filter out low-quality cells (doublets and/or mitochondrial genes). To detect and remove doublets, the distribution of the total number of unique molecular identifier (UMI) of each cell was computed for the three libraries. The filtering threshold used corresponded to the 99th percentile of the distribution. Hence, the threshold was 32,883 UMIs for the 3′ mRNA library, 740 UMIs for the ADT library, and 3,234 UMIs for the HTO library. Further, we filtered out cells with >5% mitochondrial gene contamination (indicating possibly poor quality or dying cells). PCA of the datasets were performed with Seurat R package Satija Lab, v2.2 (Satija et al., 2015). The three first PCs, containing the highest SD, were further used to run a UMAP nonlinear dimensional reduction. UMAP coordinates were subsequently visualized with Loupe browser (10X Genomics) for further analysis.

The Loupe browser was used to "label" and export the cell population of interest. The Loupe manual filtering option, using the PC1-PC2 genes or K-means clustering (K = 2 or 3), was used to identify proliferative and quiescent cells on the UMAP. Given that both approaches gave similar results, we decided to proceed further using K-means clustering, which allowed a more precise definition of the border of the proliferative and quiescent populations.

Single-cell heatmaps were obtained by using R Seurat package. The 30 top negative and 30 top positive genes identified with PC3 were selected, and the cells were ranked based on their PC3 score. PC3-negative genes were defined as HSC-MPP2 genes as they were significantly more expressed in LT-HSCs with respect to MPP4, while PC3-positive genes were considered as lymphoid-specific genes because they were significantly more expressed in MPP4 with respect to LT-HSCs.

The lineage-priming score was calculated as follows: for each cell, a gene from the HSC/MPP2 or MPP4 signature was considered expressed when its z-score value was >1. Each HSC/MPP2 gene was counted as −1; each MPP4 gene was counted as +1. Thus, cells that expressed a predominantly HSC/MPP2 gene expression signature had an overall negative score, while those that expressed an MPP4 signature had an overall positive score.

Pathway analysis of PC1 and PC2 genes (30 top positive and 30 top negative genes) was performed at the Metascape website (http://metascape.org; Satija et al., 2015).

HPC7 cells

The HPC7 cell line was cultured in IMDM supplemented with 5% FCS, monothioglycerol (150 µM), penicillin/streptomycin, mSCF (100 ng/ml), and mIL-6 (10 ng/ml; Pinto do O et al., 1998). HPC7 cells were plated at 8×10^4 cells/ml and split every 2–3 d.

ChIP-seq

Two independent ChIP-seq experiments were performed for Helios. Proteins from 50×10^6 HPC7 cells were cross-linked in 2 mM disuccinimidyl glutarate (ChemCruz) for 45 min at room temperature. Protein-DNA cross-linking was performed in 1% paraformaldehyde for 10 min at room temperature followed by addition of 2 M glycine for 5 min at room temperature to quench. Cell lysis was performed in the presence of a protease inhibitor cocktail (#11836153001; Roche) as follows: 10 min at 4°C with LB1 buffer (50 mM Tris-HCl, pH 8, 2 mM EDTA, 0.1% NP-40, and 10% glycerol) followed by 10 min at 4°C with pre-chilled LB2 buffer (10 mM Tris-HCl, pH 8, 1 mM EDTA, 0.5 mM EGTA, and 200 mM NaCl). Nuclei were resuspended in LB2.3 (18 mM Tris-HCl, pH 8, 1 mM EDTA, 0.5 mM EGTA, 200 mM NaCl, 0.033% Na-deoxycholate, and 0.16% N-laurylsarcosine) and sonicated for six cycles (5 min high, 15 s on/15 s off) with a Bioruptor (Diagenode). The sonicated chromatin was diluted 10 times into a dilution buffer (50 mM Tris-HCl, pH 8, 200 mM NaCl, 5 mM EDTA, and 0.5% NP-40) and precleared for 1 h at 4°C. The cleared chromatin was incubated ON at 4°C with a rabbit monoclonal anti-Helios Ab (Cell Signaling). Immunoprecipitation was performed with protein A-Sepharose beads

(Sigma-Aldrich) in the presence of 0.1% SDS for 1 h at 4°C. Immunoprecipitated complexes were washed six times in washing buffer (20 mM Tris-HCl, pH 8, 500 mM NaCl, 2 mM EDTA, 1% NP-40, and 0.1% SDS) and three times in 10 mM Tris-HCl, pH 8, 1mM EDTA. The immunoprecipitated complexes were eluted in 2% SDS in 10 mM Tris-HCl, pH 8, 1mM EDTA for 1 min at room temperature. De-cross-linking was performed in the elution buffer ON at 65°C, whereas the input chromatin was de-cross-linked in 200 mM NaCl in the same condition. DNA was purified using MinElute PCR Purification Kit (Qiagen). Libraries were prepared using the MicroPlex Library Preparation Kit v2 (#C05010014; Diagenode) following the manufacturer's instructions. Single-end 50-bp sequences were obtained with the HiSeq 4000. Image analysis and base calling were performed using RTA 2.7.7 and bcl2fastq 2.17.1.14. Adapter-dimer reads were removed using DimerRemover (https://sourceforge.net/projects/dimerremover/). The reads were aligned to mm10 using Bowtie. Reads overlapping the ENCODE blacklist regions were removed before peak calling. Peak calling was run using the ENCODE ChIP-seq pipeline v1.6.1*. Briefly, spp v1.15.5 was used to detect ∼300,000 peaks (Kharchenko et al., 2008), and Irreproducible Discovery Rate software was used to select reproducible peaks with an Irreproducible Discovery Rate threshold of ≤0.05 (Li et al., 2011). This resulted in an "Optimal" set of 27,020 peaks commonly detected in both experiments. We further refined the peak list by intersecting it with 16,522 peaks called by MACS v2.2.4 in the replicate with the highest signal to noise ratio, yielding a final list of 15,704 peaks.

To assign a gene to a given peak, we identified the RefSeq gene with the closest exon to the peak, using Bedtools closest v2.26.0 with the parameters «-t "first" -D "b"» and custom R scripts, as well as the RefSeq gene with the closest transcription start site, using Homer annotatePeaks.pl v4.11.1. Depending on the results of these assignments, a given peak was then associated with either one or two genes.

Fast-ATAC-seq and data analysis

5×10^4 LSK cells from WT and KO 10-wk-old mice (2 each) were used for fast-ATAC-seq (Corces et al., 2017). Briefly, cells were pelleted by centrifugation at 500*g* for 5 min at 4°C and resuspended in 50 µl transposase mixture (25 µl 2x TD buffer, 2.5 µl TDE1, 0.5 µl 1% digitonin, and 22 µl nuclease-free water; FC-121-1030, Illumina; G9441; Promega). Transposition reactions were performed at 37°C for 30 min under agitation at 300 rpm. Transposed DNA was purified using MinElute PCR Purification Kit (Qiagen) and eluted in 20 µl elution buffer. Tagmented fragments were amplified for 12 cycles. Paired-end 100-bp reads were obtained with the HiSeq 4000. Data were analyzed using the ENCODE ATAC-seq pipeline v1.5.1. Reads were aligned to mm10 using Bowtie, and peak calling was performed using MACS2 v2.2.4. The peaks detected in each sample were combined using Bedtools merge v2.26.0. Reads were normalized across libraries (Anders et al., 2015). Comparisons of interest were performed using the method proposed by the DESeq2 Bioconductor library (DESeq2 v1.24.0). Visualization of normalized data were generated from post-processed files using Homer make UCSC file v4.11.1 with the "-norm 3e7 -style dnase" parameter (Anders et al., 2015).

Identification of the ATAC-seq peaks bound by Helios was performed by intersecting the intervals of the Bedtools (v2.29.0; https://usegalaxy.eu) with ATAC-seq regions (KO vs. WT $P < 0.05$) and with Helios ChIP-seq peaks using a pileup >15. Motif research was performed at the MEME (http://meme-suite.org/) using Discriminative Regular Expression Motif Elicitation v5.1.1. Data were visualized using Integrative Genomic Viewer (IGV_2.6.2) and seqMINER_1.3.3g. Pathway analyses were performed at the Metascape website (http://metascape.org).

Online supplemental material

Fig. S1 shows the impact of Helios deficiency on mature BM hematopoietic populations. Fig. S2 shows BM inflammation phenotype of Helios-KO mice. Fig. S3 shows the transcriptome of $CD34^-Flt3^-$ LT-HSCs, Helios expression in young and old mice, and Ikaros expression in KO HSPCs. Fig. S4 shows genomic analysis of Helios function in HPC7 and LSK cells. Fig. S5 shows PCAs of single-cell RNA-seq and comparison of HSPCs using protein versus mRNA expression. Table S1 lists genes deregulated in Helios-KO LT-HSCs and MPP3 and MPP4 cells. Table S2 lists Abs, viability dyes, and reagents used for FACS staining.

Data availability

Sequencing data from this study have been deposited in the GEO database under accession code GSE149354.

Acknowledgments

We thank members of the Chan-Kastner laboratory for scientific discussion and help and P. Marchal for technical support. We thank Steve Emerson for critical discussions. We thank C. Keime and D. Dembélé for help with the RNA-seq data analysis, the IGBMC GenomEast platform for help with microarrays and sequencing, the IGBMC flow cytometry facility (C. Ebel), the IGBMC animal facility (M. Gendron, S. Falcone, W. Magnant, and A. Vincent), and the IGBMC cell culture facility.

S. Chan and P. Kastner received funding from the Agence Nationale de la Recherche (ANR; ANR-11-BSV3-018-01 and ANR-17-CE15-0023-01); the Institut National du Cancer (INCa; PLBIO-2015-114); Ligue Nationale Contre le Cancer (LNCC; Equipe Labellisée 2015-2017); Fondation pour la Recherche Médicale (FRM; Equipe FRM 2019, EQU201903007812); Fondation ARC; LNCC Grand Est/Bourgogne Franche Comté; institute funds from INSERM, CNRS, Université de Strasbourg, and the institute grant ANR-10-LABX-0030-INRT, a French State fund managed by the ANR under the frame program Investissements d'Avenir ANR-10-IDEX-0002-02; and an LNCC Grand Est/Bourgogne Franche Comté equipment grant (001K.2016). G. Cova and M.-C. Deau received predoctoral fellowships from the IGBMC International PhD Programme funded by the ANR grant ANR-10-LABX-0030-INRT, and the FRM. C. Taroni was supported by predoctoral funds from the European Union's Horizon 2020 research and innovation program under the Marie Sklodowska-Curie grant agreement 813091. G. Cova received postdoctoral funding from the ANR grant ANR-17-CE15-0023-01. Q. Cai received a Fondation ARC predoctoral fellowship and postdoctoral funding from the INCa grant PLBIO-2015-114.

Author contributions: G. Cova, C. Taroni, M.-C. Deau, Q. Cai, V. Mittelheisser, M. Philipps, and P. Kirstetter performed experiments. G. Cova, C. Taroni, M.-C. Deau, Q. Cai, V. Mittelheisser, P. Kirstetter, P. Kastner, and S. Chan analyzed data. M. Jung, M. Cerciat, S. Le Gras, C. Thibault-Carpentier, and B. Jost performed and analyzed high-throughput sequencing. L. Carlsson, A.M. Thornton, and E.M. Shevach contributed essential reagents. P. Kirstetter, P. Kastner, and S. Chan supervised the work. G. Cova, P. Kirstetter, P. Kastner, and S. Chan designed the study and wrote the manuscript.

Disclosures: The authors declare no competing interests exist.

Submitted: 30 October 2020
Revised: 28 May 2021
Accepted: 27 July 2021

References

Akashi, K., D. Traver, T. Miyamoto, and I.L. Weissman. 2000. A clonogenic common myeloid progenitor that gives rise to all myeloid lineages. *Nature.* 404:193–197. https://doi.org/10.1038/35004599

Allman, D., A. Sambandam, S. Kim, J.P. Miller, A. Pagan, D. Well, A. Meraz, and A. Bhandoola. 2003. Thymopoiesis independent of common lymphoid progenitors. *Nat. Immunol.* 4:168–174. https://doi.org/10.1038/ni878

Anders, S., P.T. Pyl, and W. Huber. 2015. HTSeq--a Python framework to work with high-throughput sequencing data. *Bioinformatics.* 31:166–169. https://doi.org/10.1093/bioinformatics/btu638

Aurrand-Lions, M., and S.J.C. Mancini. 2018. Murine Bone Marrow Niches from Hematopoietic Stem Cells to B Cells. *Int. J. Mol. Sci.* 19:E2353. https://doi.org/10.3390/ijms19082353

Badea, T.C., Z.L. Hua, P.M. Smallwood, J. Williams, T. Rotolo, X. Ye, and J. Nathans. 2009. New mouse lines for the analysis of neuronal morphology using CreER(T)/loxP-directed sparse labeling. *PLoS One.* 4: e7859. https://doi.org/10.1371/journal.pone.0007859

Busch, K., K. Klapproth, M. Barile, M. Flossdorf, T. Holland-Letz, S.M. Schlenner, M. Reth, T. Höfer, and H.-R. Rodewald. 2015. Fundamental properties of unperturbed haematopoiesis from stem cells in vivo. *Nature.* 518:542–546. https://doi.org/10.1038/nature14242

Butler, A., P. Hoffman, P. Smibert, E. Papalexi, and R. Satija. 2018. Integrating single-cell transcriptomic data across different conditions, technologies, and species. *Nat. Biotechnol.* 36:411–420. https://doi.org/10.1038/nbt.4096

Cai, Q., A. Dierich, M. Oulad-Abdelghani, S. Chan, and P. Kastner. 2009. Helios deficiency has minimal impact on T cell development and function. *J. Immunol.* 183:2303–2311. https://doi.org/10.4049/jimmunol.0901407

Carrelha, J., Y. Meng, L.M. Kettyle, T.C. Luis, R. Norfo, V. Alcolea, H. Boukarabila, F. Grasso, A. Gambardella, A. Grover, et al. 2018. Hierarchically related lineage-restricted fates of multipotent haematopoietic stem cells. *Nature.* 554:106–111. https://doi.org/10.1038/nature25455

Chen, C., W. Yu, J. Tober, P. Gao, B. He, K. Lee, T. Trieu, G.A. Blobel, N.A. Speck, and K. Tan. 2019. Spatial Genome Re-organization between Fetal and Adult Hematopoietic Stem Cells. *Cell Rep.* 29:4200–4211.e7. https://doi.org/10.1016/j.celrep.2019.11.065

Corces, M.R., A.E. Trevino, E.G. Hamilton, P.G. Greenside, N.A. Sinnott-Armstrong, S. Vesuna, A.T. Satpathy, A.J. Rubin, K.S. Montine, B. Wu, et al. 2017. An improved ATAC-seq protocol reduces background and enables interrogation of frozen tissues. *Nat. Methods.* 14:959–962. https://doi.org/10.1038/nmeth.4396

Dembélé, D., and P. Kastner. 2014. Fold change rank ordering statistics: a new method for detecting differentially expressed genes. *BMC Bioinformatics.* 15:14. https://doi.org/10.1186/1471-2105-15-14

Doré, L.C., T.M. Chlon, C.D. Brown, K.P. White, and J.D. Crispino. 2012. Chromatin occupancy analysis reveals genome-wide GATA factor switching during hematopoiesis. *Blood.* 119:3724–3733. https://doi.org/10.1182/blood-2011-09-380634

Drissen, R., N. Buza-Vidas, P. Woll, S. Thongjuea, A. Gambardella, A. Giustacchini, E. Mancini, A. Zriwil, M. Lutteropp, A. Grover, et al. 2016. Distinct myeloid progenitor-differentiation pathways identified through single-cell RNA sequencing. *Nat. Immunol.* 17:666–676. https://doi.org/10.1038/ni.3412

Estevez, B., S. Borst, D. Jarocha, V. Sudunagunta, M. Gonzalez, J. Garifallou, H. Hakonarson, P. Gao, K. Tan, P. Liu, et al. 2021. RUNX-1 haploinsufficiency causes a marked deficiency of megakaryocyte-biased hematopoietic progenitor cells. *Blood.* 137:2662–2675. https://doi.org/10.1182/blood.2020006389

Gekas, C., and T. Graf. 2013. CD41 expression marks myeloid-biased adult hematopoietic stem cells and increases with age. *Blood.* 121:4463–4472. https://doi.org/10.1182/blood-2012-09-457929

Grover, A., A. Sanjuan-Pla, S. Thongjuea, J. Carrelha, A. Giustacchini, A. Gambardella, I. Macaulay, E. Mancini, T.C. Luis, A. Mead, et al. 2016. Single-cell RNA sequencing reveals molecular and functional platelet bias of aged haematopoietic stem cells. *Nat. Commun.* 7:11075. https://doi.org/10.1038/ncomms11075

Haas, S., J. Hansson, D. Klimmeck, D. Loeffler, L. Velten, H. Uckelmann, S. Wurzer, Á.M. Prendergast, A. Schnell, K. Hexel, et al. 2015. Inflammation-Induced Emergency Megakaryopoiesis Driven by Hematopoietic Stem Cell-like Megakaryocyte Progenitors. *Cell Stem Cell.* 17:422–434. https://doi.org/10.1016/j.stem.2015.07.007

Hirata, Y., K. Furuhashi, H. Ishii, H.W. Li, S. Pinho, L. Ding, S.C. Robson, P.S. Frenette, and J. Fujisaki. 2018. CD150^{high} Bone Marrow Tregs Maintain Hematopoietic Stem Cell Quiescence and Immune Privilege via Adenosine. *Cell Stem Cell.* 22:445–453.e5. https://doi.org/10.1016/j.stem.2018.01.017

Ichikawa, M., T. Asai, T. Saito, S. Seo, I. Yamazaki, T. Yamagata, K. Mitani, S. Chiba, S. Ogawa, M. Kurokawa, and H. Hirai. 2004. AML-1 is required for megakaryocytic maturation and lymphocytic differentiation, but not for maintenance of hematopoietic stem cells in adult hematopoiesis. *Nat. Med.* 10:299–304. https://doi.org/10.1038/nm997

ImmGen Consortium. 2016. Open-source ImmGen: mononuclear phagocytes. *Nat. Immunol.* 17:741. https://doi.org/10.1038/ni.3478

Kharchenko, P.V., M.Y. Tolstorukov, and P.J. Park. 2008. Design and analysis of ChIP-seq experiments for DNA-binding proteins. *Nat. Biotechnol.* 26: 1351–1359. https://doi.org/10.1038/nbt.1508

Li, Q., J.B. Brown, H. Huang, and P.J. Bickel. 2011. Measuring reproducibility of high-throughput experiments. *Ann. Appl. Stat.* 5:1752–1779. https://doi.org/10.1214/11-AOAS466

Liang, Z., K.E. Brown, T. Carroll, B. Taylor, I.F. Vidal, B. Hendrich, D. Rueda, A.G. Fisher, and M. Merkenschlager. 2017. A high-resolution map of transcriptional repression. *eLife.* 6:e22767. https://doi.org/10.7554/eLife.22767

Liu, A., S. Li, V. Donnenberg, J. Fu, S.M. Gollin, H. Ma, C. Lu, D.B. Stolz, M.Y. Mapara, S.A. Monaghan, and S. Lentzsch. 2018. Immunomodulatory drugs downregulate IKZF1 leading to expansion of hematopoietic progenitors with concomitant block of megakaryocytic maturation. *Haematologica.* 103:1688–1697. https://doi.org/10.3324/haematol.2018.188227

Malinge, S., C. Thiollier, T.M. Chlon, L.C. Doré, L. Diebold, O. Bluteau, V. Mabialah, W. Vainchenker, P. Dessen, S. Winandy, et al. 2013. Ikaros inhibits megakaryopoiesis through functional interaction with GATA-1 and NOTCH signaling. *Blood.* 121:2440–2451. https://doi.org/10.1182/blood-2012-08-450627

Martinez-Høyer, S., Y. Deng, J. Parker, J. Jiang, A. Mo, T.R. Docking, N. Gharaee, J. Li, P. Umlandt, M. Fuller, et al. 2020. Loss of lenalidomide-induced megakaryocytic differentiation leads to therapy resistance in del(5q) myelodysplastic syndrome. *Nat. Cell Biol.* 22:526–533. https://doi.org/10.1038/s41556-020-0497-9

Martins, V.C., K. Busch, D. Juraeva, C. Blum, C. Ludwig, V. Rasche, F. Lasitschka, S.E. Mastitsky, B. Brors, T. Hielscher, et al. 2014. Cell competition is a tumour suppressor mechanism in the thymus. *Nature.* 509: 465–470. https://doi.org/10.1038/nature13317

Mastio, J., C. Simand, G. Cova, P. Kastner, S. Chan, and P. Kirstetter. 2018. Ikaros cooperates with Notch activation and antagonizes TGFβ signaling to promote pDC development. *PLoS Genet.* 14:e1007485. https://doi.org/10.1371/journal.pgen.1007485

Mirantes, C., E. Passegué, and E.M. Pietras. 2014. Pro-inflammatory cytokines: emerging players regulating HSC function in normal and diseased hematopoiesis. *Exp. Cell Res.* 329:248–254. https://doi.org/10.1016/j.yexcr.2014.08.017

Ng, S.Y.-M., T. Yoshida, J. Zhang, and K. Georgopoulos. 2009. Genome-wide lineage-specific transcriptional networks underscore Ikaros-dependent lymphoid priming in hematopoietic stem cells. *Immunity.* 30:493–507. https://doi.org/10.1016/j.immuni.2009.01.014

Nichogiannopoulou, A., M. Trevisan, S. Neben, C. Friedrich, and K. Georgopoulos. 1999. Defects in hemopoietic stem cell activity in Ikaros mutant mice. *J. Exp. Med.* 190:1201–1214. https://doi.org/10.1084/jem.190.9.1201

Oguro, H., L. Ding, and S.J. Morrison. 2013. SLAM family markers resolve functionally distinct subpopulations of hematopoietic stem cells and multipotent progenitors. *Cell Stem Cell.* 13:102–116. https://doi.org/10.1016/j.stem.2013.05.014

Oravecz, A., A. Apostolov, K. Polak, B. Jost, S. Le Gras, S. Chan, and P. Kastner. 2015. Ikaros mediates gene silencing in T cells through Polycomb repressive complex 2. *Nat. Commun.* 6:8823. https://doi.org/10.1038/ncomms9823

Park, S.-M., H. Cho, A.M. Thornton, T.S. Barlowe, T. Chou, S. Chhangawala, L. Fairchild, J. Taggart, A. Chow, A. Schurer, et al. 2019. IKZF2 Drives Leukemia Stem Cell Self-Renewal and Inhibits Myeloid Differentiation. *Cell Stem Cell.* 24:153–165.e7. https://doi.org/10.1016/j.stem.2018.10.016

Pencovich, N., R. Jaschek, A. Tanay, and Y. Groner. 2011. Dynamic combinatorial interactions of RUNX1 and cooperating partners regulates megakaryocytic differentiation in cell line models. *Blood.* 117:e1–e14. https://doi.org/10.1182/blood-2010-07-295113

Pietras, E.M., D. Reynaud, Y.-A. Kang, D. Carlin, F.J. Calero-Nieto, A.D. Leavitt, J.M. Stuart, B. Göttgens, and E. Passegué. 2015. Functionally Distinct Subsets of Lineage-Biased Multipotent Progenitors Control Blood Production in Normal and Regenerative Conditions. *Cell Stem Cell.* 17:35–46. https://doi.org/10.1016/j.stem.2015.05.003

Pimkin, M., A.V. Kossenkov, T. Mishra, C.S. Morrissey, W. Wu, C.A. Keller, G.A. Blobel, D. Lee, M.A. Beer, R.C. Hardison, and M.J. Weiss. 2014. Divergent functions of hematopoietic transcription factors in lineage priming and differentiation during erythro-megakaryopoiesis. *Genome Res.* 24:1932–1944. https://doi.org/10.1101/gr.164178.113

Pinho, S., and P.S. Frenette. 2019. Haematopoietic stem cell activity and interactions with the niche. *Nat. Rev. Mol. Cell Biol.* 20:303–320. https://doi.org/10.1038/s41580-019-0103-9

Pinto do O, P., A. Kolterud, and L. Carlsson. 1998. Expression of the LIM-homeobox gene LH2 generates immortalized steel factor-dependent multipotent hematopoietic precursors. *EMBO J.* 17:5744–5756. https://doi.org/10.1093/emboj/17.19.5744

Pulecio, J., O. Alejo-Valle, S. Capellera-Garcia, M. Vitaloni, P. Rio, E. Mejía-Ramírez, I. Caserta, J.A. Bueren, J. Flygare, and A. Raya. 2016. Direct Conversion of Fibroblasts to Megakaryocyte Progenitors. *Cell Rep.* 17:671–683. https://doi.org/10.1016/j.celrep.2016.09.036

Rodriguez-Fraticelli, A.E., S.L. Wolock, C.S. Weinreb, R. Panero, S.H. Patel, M. Jankovic, J. Sun, R.A. Calogero, A.M. Klein, and F.D. Camargo. 2018. Clonal analysis of lineage fate in native haematopoiesis. *Nature.* 553:212–216. https://doi.org/10.1038/nature25168

Sanjuan-Pla, A., I.C. Macaulay, C.T. Jensen, P.S. Woll, T.C. Luis, A. Mead, S. Moore, C. Carella, S. Matsuoka, T. Bouriez Jones, et al. 2013. Platelet-biased stem cells reside at the apex of the haematopoietic stem-cell hierarchy. *Nature.* 502:232–236. https://doi.org/10.1038/nature12495

Satija, R., J.A. Farrell, D. Gennert, A.F. Schier, and A. Regev. 2015. Spatial reconstruction of single-cell gene expression data. *Nat. Biotechnol.* 33:495–502. https://doi.org/10.1038/nbt.3192

Sebastian, M., M. Lopez-Ocasio, A. Metidji, S.A. Rieder, E.M. Shevach, and A.M. Thornton. 2016. Helios Controls a Limited Subset of Regulatory T Cell Functions. *J. Immunol.* 196:144–155. https://doi.org/10.4049/jimmunol.1501704

Seita, J., and I.L. Weissman. 2010. Hematopoietic stem cell: self-renewal versus differentiation. *Wiley Interdiscip. Rev. Syst. Biol. Med.* 2:640–653. https://doi.org/10.1002/wsbm.86

Sridharan, R., and S.T. Smale. 2007. Predominant interaction of both Ikaros and Helios with the NuRD complex in immature thymocytes. *J. Biol. Chem.* 282:30227–30238. https://doi.org/10.1074/jbc.M702541200

Stoeckius, M., C. Hafemeister, W. Stephenson, B. Houck-Loomis, P.K. Chattopadhyay, H. Swerdlow, R. Satija, and P. Smibert. 2017. Simultaneous epitope and transcriptome measurement in single cells. *Nat. Methods.* 14:865–868. https://doi.org/10.1038/nmeth.4380

Stoeckius, M., S. Zheng, B. Houck-Loomis, S. Hao, B.Z. Yeung, W.M. Mauck III, P. Smibert, and R. Satija. 2018. Cell Hashing with barcoded antibodies enables multiplexing and doublet detection for single cell genomics. *Genome Biol.* 19:224. https://doi.org/10.1186/s13059-018-1603-1

Subramanian, A., P. Tamayo, V.K. Mootha, S. Mukherjee, B.L. Ebert, M.A. Gillette, A. Paulovich, S.L. Pomeroy, T.R. Golub, E.S. Lander, and J.P. Mesirov. 2005. Gene set enrichment analysis: a knowledge-based approach for interpreting genome-wide expression profiles. *Proc. Natl. Acad. Sci. USA.* 102:15545–15550. https://doi.org/10.1073/pnas.0506580102

Sun, D., M. Luo, M. Jeong, B. Rodriguez, Z. Xia, R. Hannah, H. Wang, T. Le, K.F. Faull, R. Chen, et al. 2014. Epigenomic profiling of young and aged HSCs reveals concerted changes during aging that reinforce self-renewal. *Cell Stem Cell.* 14:673–688. https://doi.org/10.1016/j.stem.2014.03.002

Thornton, A.M., and E.M. Shevach. 2019. Helios: still behind the clouds. *Immunology.* 158:161–170. https://doi.org/10.1111/imm.13115

Tijssen, M.R., and C. Ghevaert. 2013. Transcription factors in late megakaryopoiesis and related platelet disorders. *J. Thromb. Haemost.* 11:593–604. https://doi.org/10.1111/jth.12131

Trinh, L.A., R. Ferrini, B.S. Cobb, A.S. Weinmann, K. Hahm, P. Ernst, I.P. Garraway, M. Merkenschlager, and S.T. Smale. 2001. Down-regulation of TDT transcription in CD4(+)CD8(+) thymocytes by Ikaros proteins in direct competition with an Ets activator. *Genes Dev.* 15:1817–1832. https://doi.org/10.1101/gad.905601

Wang, Z., and H. Ema. 2016. Mechanisms of self-renewal in hematopoietic stem cells. *Int. J. Hematol.* 103:498–509. https://doi.org/10.1007/s12185-015-1919-5

Wilkinson, A.C., and B. Göttgens. 2013. Transcriptional regulation of haematopoietic stem cells. *Adv. Exp. Med. Biol.* 786:187–212. https://doi.org/10.1007/978-94-007-6621-1_11

Wilson, N.K., S.D. Foster, X. Wang, K. Knezevic, J. Schütte, P. Kaimakis, P.M. Chilarska, S. Kinston, W.H. Ouwehand, E. Dzierzak, et al. 2010. Combinatorial transcriptional control in blood stem/progenitor cells: genome-wide analysis of ten major transcriptional regulators. *Cell Stem Cell.* 7:532–544. https://doi.org/10.1016/j.stem.2010.07.016

Wolfer, A., T. Bakker, A. Wilson, M. Nicolas, V. Ioannidis, D.R. Littman, P.P. Lee, C.B. Wilson, W. Held, H.R. MacDonald, and F. Radtke. 2001. Inactivation of Notch 1 in immature thymocytes does not perturb CD4 or CD8T cell development. *Nat. Immunol.* 2:235–241. https://doi.org/10.1038/85294

Yoshida, T., S.Y.-M. Ng, J.C. Zuniga-Pflucker, and K. Georgopoulos. 2006. Early hematopoietic lineage restrictions directed by Ikaros. *Nat. Immunol.* 7:382–391. https://doi.org/10.1038/ni1314

Zhou, Y., B. Zhou, L. Pache, M. Chang, A.H. Khodabakhshi, O. Tanaseichuk, C. Benner, and S.K. Chanda. 2019. Metascape provides a biologist-oriented resource for the analysis of systems-level datasets. *Nat. Commun.* 10:1523. https://doi.org/10.1038/s41467-019-09234-6

JEM

Supplemental material

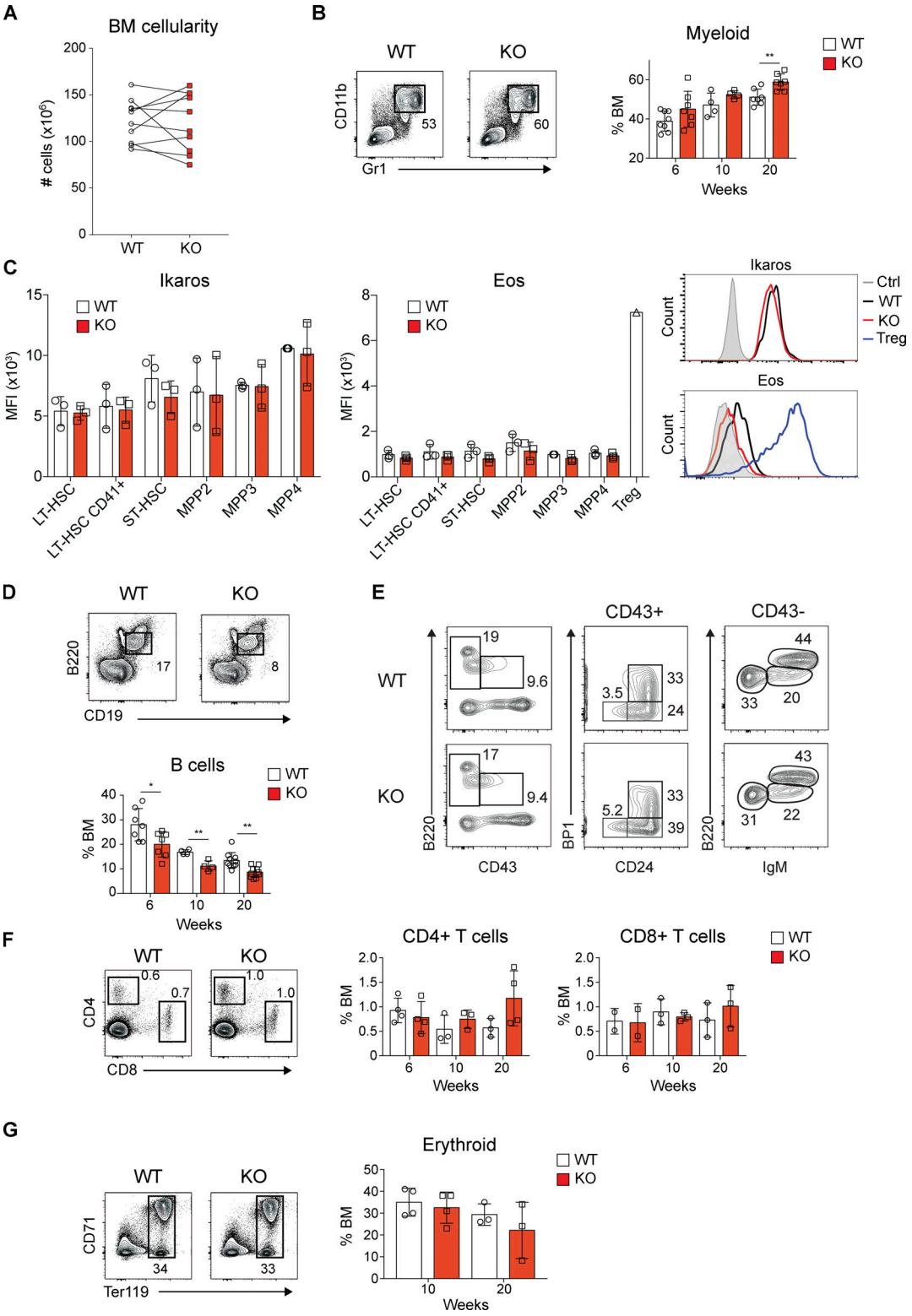

Figure S1. **Impact of Helios deficiency on mature BM hematopoietic populations. (A)** Combined BM cellularity of tibias, femurs, pelvis, and sternum from 10-wk-old WT and KO mice (females and males). Lines connect samples from the same experiment. **(B)** Representative contour plots depicting myeloid cells and their relative percentages in 6-, 10-, and 20-wk-old mice. Mean ± SD of two to seven independent experiments. **(C)** Graphs showing the MFI for Ikaros and Eos in the indicated populations from WT and KO mice. Mean ± SD of three independent experiments. Representative histograms are shown on the right. Splenic Treg cells were used a positive control for Eos expression. **(D and E)** Representative contour plots depicting B cells and their relative percentages as in B, and B cell development using the Hardy classification scheme. **(F)** Representative contour plots depicting CD4$^+$ and CD8$^+$ T cells and their relative percentages as in B. **(G)** Representative contour plots depicting indicated populations as in B for the erythroid population (quantification only for 10- and 20-wk-old mice). Unpaired two-tailed *t* test: *, P < 0.05; **, P < 0.01.

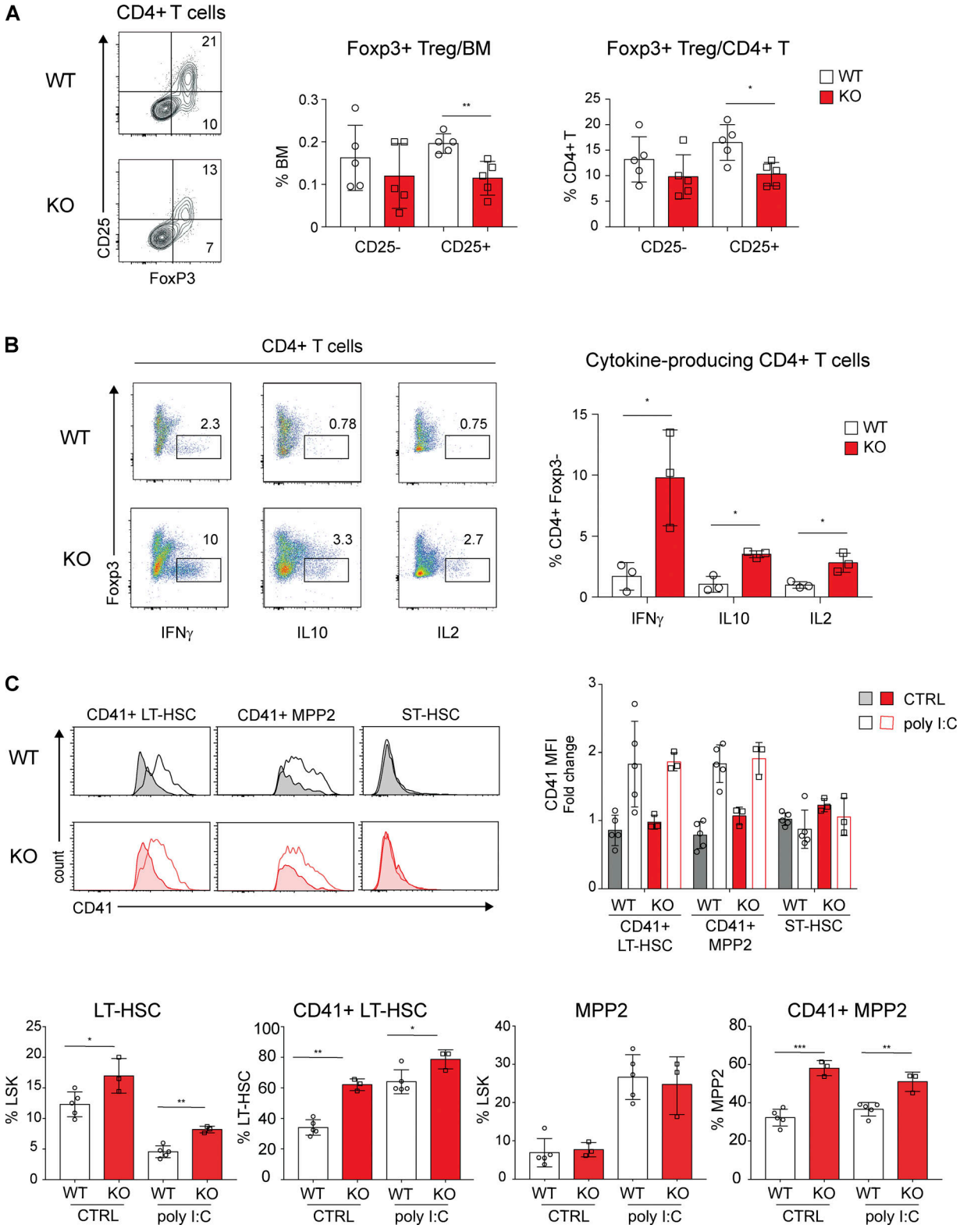

Figure S2. **BM inflammation phenotype of Helios-KO mice. (A)** Representative contour plot of the indicated BM populations, and their relative quantification in 10–20-wk-old mice. **(B)** Representative dot plot of cytokine staining from enriched and stimulated BM CD4⁺ T cells (see Materials and methods) of 6-, 10-, and 20-wk-old mice. Mean ± SD of four independent experiments. Unpaired two-tailed *t* test: *, P < 0.05; **, P < 0.01. **(C)** Representative histograms of CD41 expression in the indicated populations of WT and KO mice 16 h after poly I:C challenge. CD41 MFI FC was assessed in WT and KO populations from poly I:C– or control-treated mice. Relative quantification of indicated BM populations of WT and KO mice from control and poly I:C–treated mice. Mean ± SD of five independent experiments. Unpaired two-tailed *t* test: *, P < 0.05; **, P < 0.01; ***, P < 0.001.

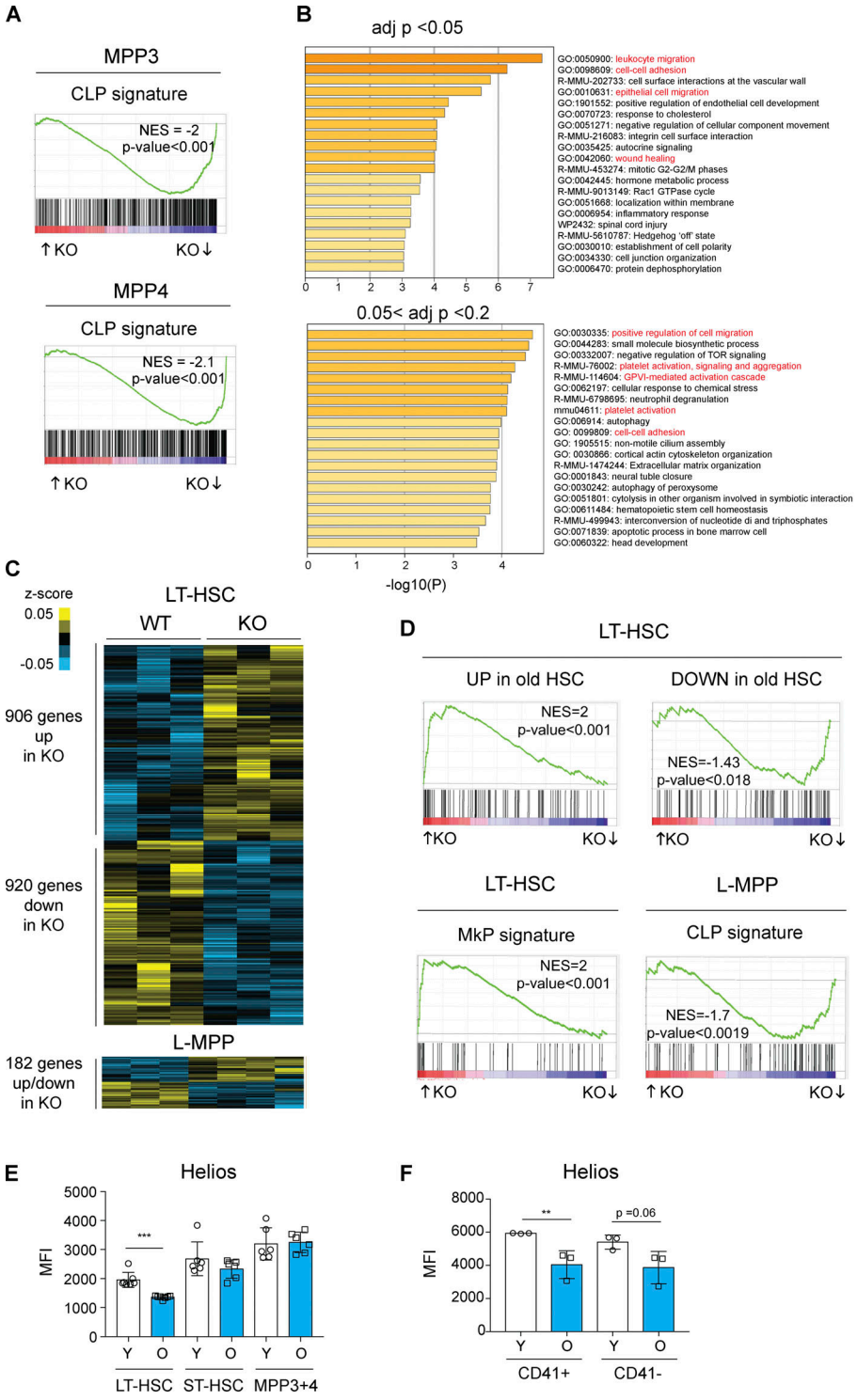

Figure S3. **Transcriptome of CD34⁻Flt3⁻ LT-HSCs, Helios expression in young and old mice, and Ikaros expression in KO HSPCs. (A)** GSEA of the CLP signature among genes deregulated in KO versus WT MPP3 and MPP4 cells. Ranked gene lists comprise all genes detected in the RNA-seq experiments, ranked according to their FC (KO vs. WT). CLP signature genes (Grover et al., 2016) were used as gene sets. The NES and P values are shown for each analysis. **(B)** Metascape enrichment analysis for the genes deregulated in Helios-KO LT-HSCs (selected from the analysis shown in Fig. 6 A), after separation into groups meeting stringent (adj P < 0.05) and mild 0.05< adj P < 0.2) statistical criteria. **(C)** Heatmap of up- and down-regulated genes in WT and KO LT-HSCs (CD34⁻Flt3⁻ LSK) and L-MPPs (CD34⁺Flt3⁺ LSK), analyzed with Affymetrix 430 2.0 microarrays. **(D)** GSEA of LT-HSCs and L-MPP (CD34⁺Flt3⁺ LSK) cells, using as ranked lists up- and down-regulated genes (KO vs. WT, P value<0.05). Signature lists of MkP and CLP (Grover et al., 2016) and up- and down-regulated genes in old HSCs (Sun et al., 2014) were used as gene sets. NES and P values are shown for each analysis. **(E)** Relative Helios protein levels in the indicated HSPC populations of young (10-wk-old) and old (>1-yr-old) WT mice, as determined by MFI of flow cytometry results of six independent experiments. **(F)** Relative Helios protein in CD41⁺ and CD41⁻ LT-HSCs of young (10-wk-old) and old (>1-yr-old) WT mice, as determined by MFI of flow cytometry results of six (from young) and three (from old) independent experiments. Unpaired two-tailed *t* test: **, P < 0.01; ***, P < 0.001.

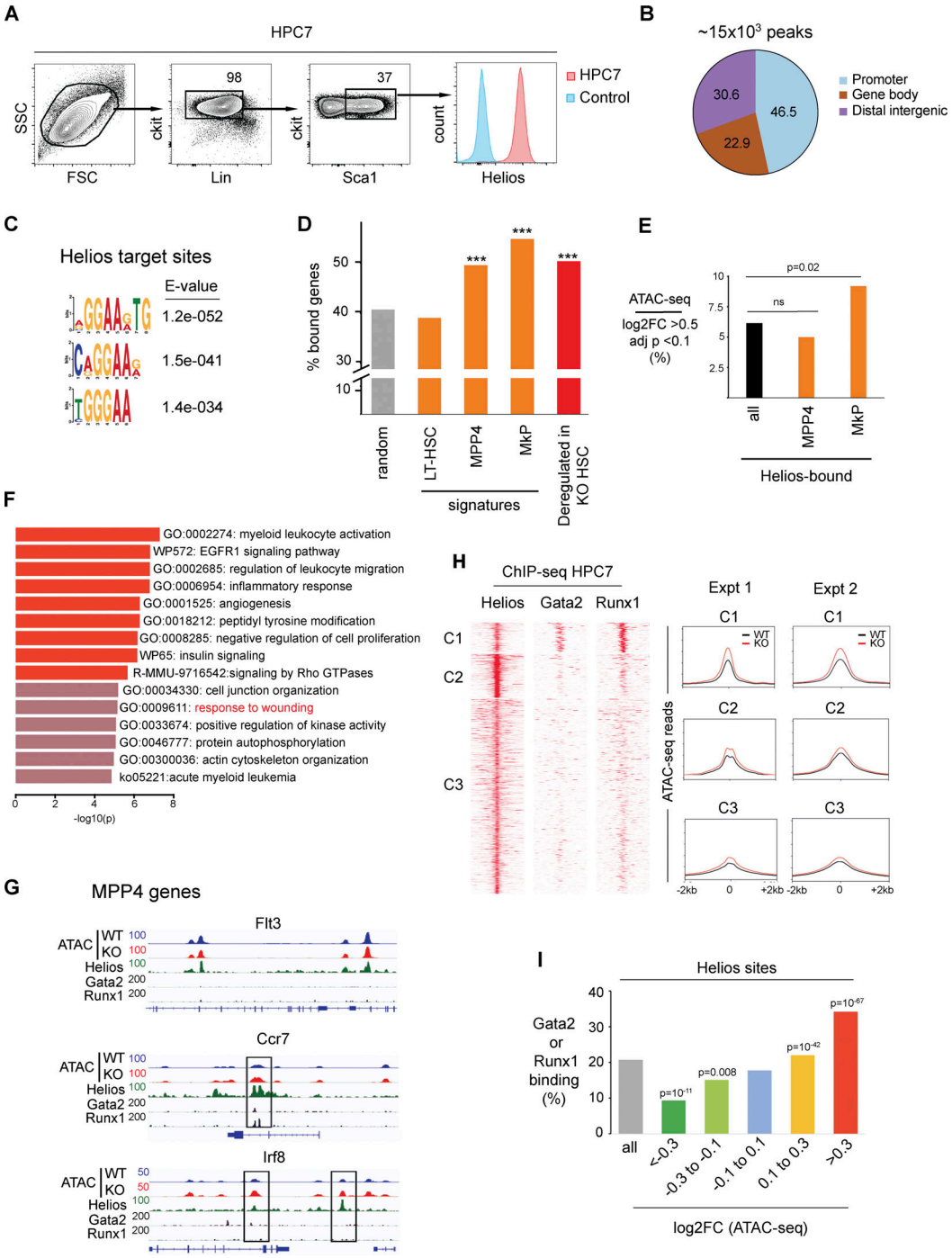

Figure S4. **Genomic analysis of Helios function in HPC7 and LSK cells. (A)** LSK and LK phenotype of HPC7 cells and Helios expression. Blue histogram corresponds to cells stained with the secondary Ab only. FSC, forward scatter; SSC, side scatter. **(B)** Helios binding across genomic regions: promoter (−3 kb from transcription start site), gene body (exons, introns, UTR), distal intergenic. **(C)** Enriched DNA motifs found within the 1000 regions with the strongest Helios binding (ranked by decreasing pileup score). **(D)** Frequency of genes bound by Helios among those from the LT-HSC, MPP4, or MkP signatures, or among genes deregulated in He KO LT-HSCs. Random sets of 500 genes were selected from genes detected in the RNA-seq experiment. Poorly defined genes (Riken genes or Gene Models, rarely bound by Helios) were excluded from the gene lists that were intersected with the list of Helios-bound genes. ***, P < 0.001 (hypergeometric test). **(E)** Proportion of Helios-bound sites with a significant increase in chromatin accessibility (ATAC log2FC > 0.5; adj P < 0.1) among all ATAC-seq peaks, or peaks associated with MPP4 or MkP genes. P values were calculated with the hypergeometric test. **(F)** Metascape analysis of the enriched pathways associated with ATAC-seq regions that were significantly increased in KO LSK cells (adj P < 0.2). **(G)** Integrative genome viewer screenshots of WT and KO LSK ATAC-seq signals, and Helios, Gata2, and Runx1 binding in HPC7 cells, for the representative MPP4 genes. **(H)** Left: Seq-miner heatmap showing Helios, Gata2, and Runx1 binding on the 10,890 Helios-bound regions that coincided with an ATAC-seq peak. Three clusters (C1–C3) were defined using K-means clustering. Right: Mean profiles of the ATAC-seq signals in peaks from clusters C1–C3, in each pair of WT/KO replicates. **(I)** Proportion of Helios sites bound by Gata2 and/or Runx1, based on the magnitude of ATAC-seq changes. P values were calculated with the hypergeometric test, using the frequency of Gata2/Runx1 binding among unchanged peaks (−0.1 < log2FC < 0.1) as a reference distribution.

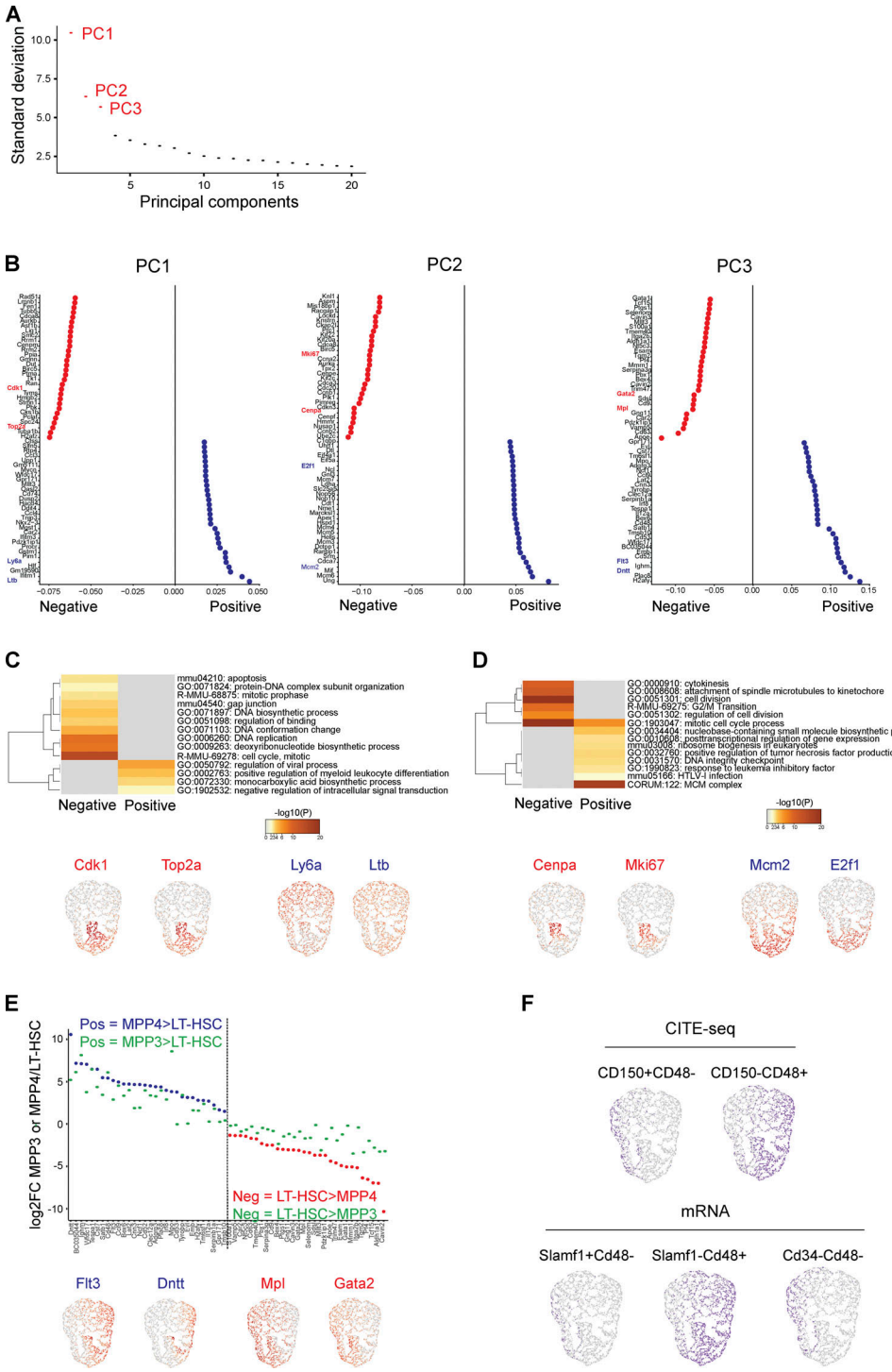

Figure S5. **PCAs of single-cell RNA-seq and comparison of HSPCs using protein vs mRNA expression. (A)** Ranking of the PC variations that define the HSPC population, (ElbowPlot function; Seurat library). PC1–PC3, which account for most of the variations, are indicated in red. **(B)** Dot plot depicting PC1–PC3 features with the top 30 negative (red) and positive (blue) genes contributing to each PC, ranked according to their relative score. **(C and D)** Top: Metascape pathway analysis of the highlighted PC1 and PC2 genes from B. Pathways associated with top negative (red) and positive (blue) PC1 genes are highlighted. Bottom: Representative examples of negative (red) and positive (blue) PC1 or PC2 genes and their expression patterns within the HSPC UMAP. The corresponding positions of these genes are shown in the dot plot in B. **(E)** Top: Comparison of gene expression values between MPP4 (or MPP3) versus LT-HSC for the PC3 genes. Genes with a positive score, expressed higher in MPP4 cells, are in blue; genes with a negative score, expressed higher in LT-HSCs, are in red. A similar analysis was performed between MPP3 and LT-HSC (green), which showed that MPP3 cells expressed PC3 genes at an intermediate level compared with LT-HSC and MPP4 cells. Bottom: Representative examples of negative (red) and positive (blue) PC3 genes and their expression patterns within the HSPC UMAP. The corresponding positions of these genes are shown in the dot plot in B. **(F)** Left: UMAPs depicting LT-HSC ($CD150^+CD48^-$) and MPP ($CD150^-CD48^+$) populations, as defined by their CD150 and CD48 CITE-seq Ab labeling. Right: UMAPs depicting LT-HSC ($Slamf1^+Cd48^-$ or $Cd34^-Cd48^-$) and MPP ($Slamf1^-Cd48^+$) populations, as defined by their mRNA expression.

Tables S1 and S2 are provided online as separate Excel files. Table S1 lists genes deregulated in Helios KO LT-HSCs and MPP3 and MPP4 cells. Table S2 lists Abs, viability dyes, and reagents used for FACS staining.